WILEY | Hindawi

Research Article

Joint Diagnostic Approach to Pressure and Tracer Responses from Reservoirs: An Experimental and Theoretical Study to Estimate the Accuracy of Reservoir Models

Mitsuo Matsumoto [ID] [1] **and Kazuki Sawayama** [2]

[1]*Department of Earth Resources Engineering, Faculty of Engineering, Kyushu University, 744 Motooka, Nishi-ku, Fukuoka 819-0395, Japan*
[2]*Institute for Geothermal Sciences, Kyoto University, 3088-176, Noguchibaru, Beppu, Oita 874-0903, Japan*

Correspondence should be addressed to Mitsuo Matsumoto; matsumoto@mine.kyushu-u.ac.jp

This study presents a novel perspective for improving the understanding of permeable structures at geothermal prospects by jointly diagnosing the responses of conventional pressure transient and tracer testing. The pressure and tracer responses individually yield apparent porosity–thickness products. The difference between them implies the existence of unknown dead-end features involved in a reservoir model. Laboratory experiments and numerical simulations validate this concept. Potential application to hypothetical exploration demonstrates that the logarithmic ratio of the porosity–thickness products, determined based on pressure and tracer responses, indicates the accuracy of the reservoir model to be successively updated with the progress of the exploration. The reservoir model successfully reproduced the synthetic observations regardless of the accuracy of permeable structure if different porosity–thickness products were allowed to be assumed to individually reproduce pressure and tracer responses. These porosity–thickness products coincided only if the reservoir model correctly captured the permeable structure. This novel perspective will provide strategic guides for successful exploration and development at the prospects of geothermal and, potentially, general geofluid resources.

1. Introduction

Adequate understanding of subsurface fluid flow under heterogeneous pore distribution is key to successfully resolve numerous geoscientific and engineering problems. This process requires the characterization of thermal, hydraulic, mechanical, and chemical processes, depending on the conditions of the given problems [1–3]. The heterogeneity of pore distribution is generated over a wide range of scales, including fracture networks observed at an outcrop [4–6] and faults intersecting a field [7–9], as well as physically and/or chemically heterogeneous porous layers [10, 11]. Pressure transient testing and tracer testing are conventional methods for investigating fluid flow under such conditions by observing temporal variations in pressure and tracer concentration,

respectively, on a field scale. Characterization of these observations provides essential perspectives for predicting and optimizing the fluid flow in reservoirs or aquifers [12–16].

Pressure transient testing measures pressure responses to production and/or injection to estimate several parameters, such as transmissivity, storativity, skin factor, and wellbore storage constant, referring to a proper model of fluid flow [17–21]. In the oil and gas industry, key parameters such as reservoir size, geometry, and mechanisms supporting reservoir pressure are estimated for project feasibility studies [22, 23]. The application of pressure transient testing in the geothermal industry involves providing the basis for estimating sustainable production and reinjection rates over several decades [24–26]. A great number of type curves for pressure responses have been developed by assuming diverse

conditions to express heterogeneity: leaky aquifers [27], dual-porosity models [28, 29], linear and bilinear flows associated with a fracture [30, 31], multiple interacting continua models [32, 33], fractional dimension models [34, 35], poroelastic aquifers [36], and multiple radial hydraulic fractures [37]. The models commonly used for analyzing pressure responses obey diffusion problems for both quasi-incompressible and compressible fluids by adopting a pseudo-pressure [38]. Application software such as AWTAS [39] and Saphir [23] allows to develop further flexible numerical models.

One of the typical tracer testing methods uses flowing wells, including injection and production wells. Referring to tracer concentration variations and obeying advection–dispersion problems, the direction and velocity of subsurface fluid flow, along with multiple properties such as porosity, dispersibility, hydrostratigraphy, and heat transfer characterization, have been successfully determined [40–47]. Tracers must satisfy several conditions such as detectivity, chemical stability, negligible adsorption, and absence in a natural state. For several decades, a variety of tracers have been adopted, including solid particles, ionized substances, stable isotopes, radioactive substances, organic dyes, gases, fluorocarbons, and water temperatures [48]. Reactive tracers have also been adopted in advanced techniques [49–52]. Tracer testing has been applied across a diverse range of conditions, including oil and gas [53–55] and geothermal [56–58] reservoirs. Investigating and characterizing the heterogeneity of the aforementioned physical properties is crucial for the successful modeling and forecasting of subsurface fluid flow. Accordingly, several scholars have attempted to overcome these problems by adopting novel techniques, such as multilevel–multitracer testing methods and equipment, DNA (deoxyribonucleic acid) tracers, stochastic simulations, and machine learning [11, 59].

This study presents a novel perspective for improving the understanding of permeable structures by jointly diagnosing the responses of pressure transient and tracer testing, which are separately studied in conventional approaches. Performing field experiments and advanced analysis using machine learning, Hawkins et al. [59] successfully demonstrated that heat transfer through a rock fracture with non-uniform permeability was accurately predicted by referring to tracer responses and frictional pressure loss under a steady-state condition. Herein, we focus on transient pressure responses to hydraulically survey pore volume. The pressure and tracer responses, obeying diffusion and advection–dispersion problems, respectively, individually yield the estimation of pore volumes (i.e., hydraulic and swept volumes). The difference between these pore volumes reflects the existence of dead-end features in a permeable structure that decline advection and allow only compression and expansion. We validate this concept using laboratory experiments and numerical simulations to establish the basis for applying to actual fields in future studies. Potential application is demonstrated to quantitatively estimate the accuracy of a reservoir model to be successively updated with the progress of hypothetical exploration. The perspective developed in this study will provide strategic guides for successful exploration and development at the prospects of geothermal and, potentially, general geofluid resources.

2. Concept

Let us consider two schematic examples that generate permeable structures with dead-end features: heterogeneous pore distribution and artificial inflow and outflow. We intend to reproduce the equivalent condition of the first example through the laboratory experiments and numerical simulations in Sections 3 and 4, respectively. The second example is referenced in the potential application to hypothetical exploration demonstrated in Section 5.

2.1. Heterogeneous Pore Distribution. In the first case, we consider a heterogeneous pore distribution on a relatively small scale of several meters to several tens of meters as a portion of a naturally fractured reservoir (Figure 1(a)). In general, permeable fracture networks contain numerous branches and dead ends [4–6]. For simplicity, we assume isenthalpic single-phase flow through fractures in a fully impermeable rock matrix. Upon performing a pressure transient test using wells intersecting the reservoir, the pressure variation obeying the diffusion problem propagates throughout the fracture network regardless of the branches and dead ends. By analyzing the pressure responses at the flowing or monitoring wells associated with the production and/or injection rates, the total pore volume, referred to as the hydraulic volume in Figure 1(b), is quantified and estimated as a storativity [22, 23, 26]. Structures equivalent to branches and dead ends are potentially generated along the fracture surface via a nonuniform aperture distribution [60, 61] forming an enclosed space with a narrow entrance. A fault core can branch or anastomose, sometimes with branching subsidiary faults [62].

In the same fractured reservoir as above, a tracer test is assumed to be performed using an inert tracer under quasi-steady-state conditions as conventionally performed [57, 58, 63, 64]. On a sufficiently smaller time scale than the molecular diffusion toward each branch, the flow paths of the tracer are restricted predominantly along continuous pathways, avoiding branches and dead ends. These flow paths are referred to as the swept volume in Figure 1(c). This volume can be estimated by analyzing the tracer responses associated with the production and injection rates to determine several conventional parameters such as total recovery and residence time [25]. Alternatively, a more direct and sophisticated approach involves simulating tracer responses by developing a reservoir model that has been successfully applied in various fields [65–67]. Thus, the pressure and tracer responses reflect the total hydraulic volume and partial volume swept by the tracer, respectively. In particular, the difference between these volumes indicates the volume of the dead-end features.

2.2. Artificial Inflow and Outflow. In the second case, we assume a relatively large scale of several kilometers to consider the total prospect. This case demonstrates a permeable structure with dead-end features generated by artificial inflow and outflow that restrict the flow paths of tracers, regardless of branches and dead ends in pore distribution. Consider a water-dominated reservoir with negligible
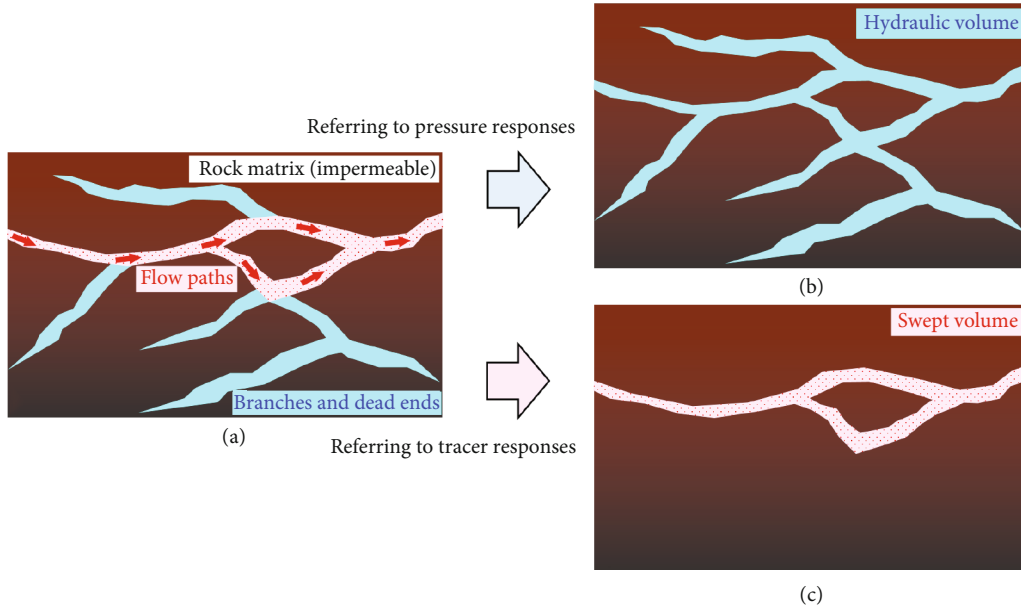
FIGURE 1: (a) Schematic of heterogeneous pore distribution consisting of flow paths and dead-end features generated by a naturally fractured reservoir. Pressure and tracer responses reflect the (b) total hydraulic volume and (c) partial volume swept by the tracer, respectively.

enthalpy variations generated by parallel-distributed steep faults with stepwise displacement (Figure 2(a)), as described by Bense et al. [68] and Cole et al. [69]. As shown in Figure 2(a), all the faults are connected to each other through the damaged zones. Fault A has been identified through ongoing hypothetical exploration, whereas faults B and C remain unknown. Accordingly, pressure transient and tracer tests are performed using the production and reinjection wells intersecting fault A. The pressure variation caused by production and reinjection propagates throughout the reservoir (i.e., hydraulic volume in Figure 2(b)), including faults B and C. An inert tracer is injected into the reinjected fluid under quasi-steady-state conditions after a sufficient period of time has elapsed since starting production and reinjection. If the production and reinjection rates are comparable to each other in particular, the tracer flow path from the reinjection to production well through fault A (i.e., swept volume in Figure 2(c)) is predominant over flow paths toward the damaged zones and other faults.

Thus, the pressure and tracer responses reflect the total hydraulic volume and partial volume swept by the tracer, respectively, when the flow paths are restricted by artificial inflow and outflow, regardless of branches and dead ends (i.e., regardless of the extension and connection of the faults and damaged zones perpendicular to Figure 2). In particular, the difference between the hydraulic and swept volumes in the case of Figure 2 implies the existence of faults B and C that remains unknown.

3. Laboratory Experiments

3.1. Methods. The concept described in Section 2 is validated through laboratory experiments. The experiments were performed assuming a quasi-Hagen–Poiseuille flow in a horizontal urethane tube, which was equivalent to a Darcy flow

in a reservoir. Connecting a buffer tank, mimicking the dead-end features, to the tube, we aimed to investigate its effects on pressure and tracer responses. In the preceding studies, successful laboratory experiments focusing on advection were presented to observe the concentrations of multiple tracers in a two-dimensional porous medium [70] and the inlet/outlet temperatures of a three-dimensionally printed fracture model [71]. We designed an experimental apparatus equipped with pressure and tracer concentration sensors, connected to a high-speed data logger, as well as solenoid valves, which enabled to accurately control and measure the variations in pressure and tracer concentration. A one-dimensional flow in the tube was assumed to numerically reproduce and characterize the observed pressure and tracer responses.

A schematic of the experimental apparatus assembled under atmospheric pressure and temperature is illustrated in Figure 3. This apparatus generated a flow of tap water under a controlled constant pressure gradient in a horizontal urethane tube with an inner diameter of 4 mm. The pressure gradient was controlled by adjusting the levels of the upstream and downstream header tanks. The flow was started by opening valve A placed upstream from the tube. At the midpoint, a cylindrical buffer tank was connected, which mimicked a branch and dead end by buffering transient pressure variations. A tracer solution (Ponceau 4R) was injected into the tube at a steady state. Detailed specifications of the experimental apparatus are provided in Appendix A. Similarity between the conditions of the laboratory experiments and reservoir models in Sections 3 and 5, respectively, was validated as presented in Appendix B.

Four experiments were performed under different conditions of the buffer tank. In the first experiment, the buffer tank was disconnected, whereas the remaining experiments were performed by connecting the buffer tank with air thicknesses of 17, 28, and 39 mm. The water levels of the
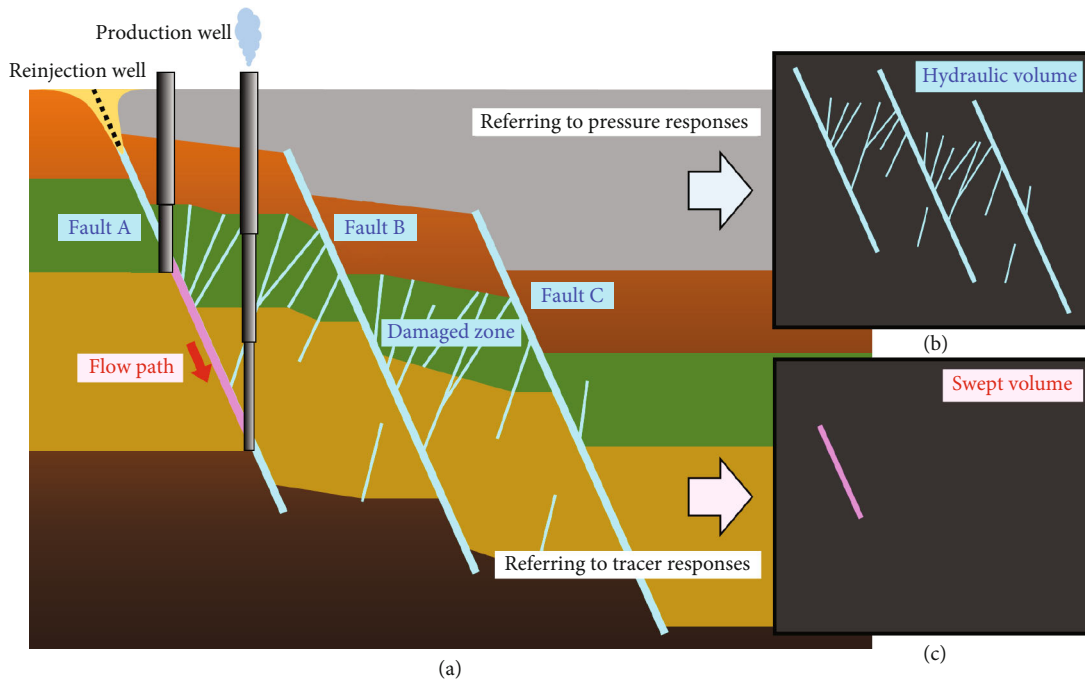
FIGURE 2: (a) Schematic of parallel-distributed steep faults connected through damaged zones. Pressure and tracer responses due to production and reinjection at fault A reflect the (b) total hydraulic volume including the other faults and (c) partial volume swept by the tracer in fault A, respectively.
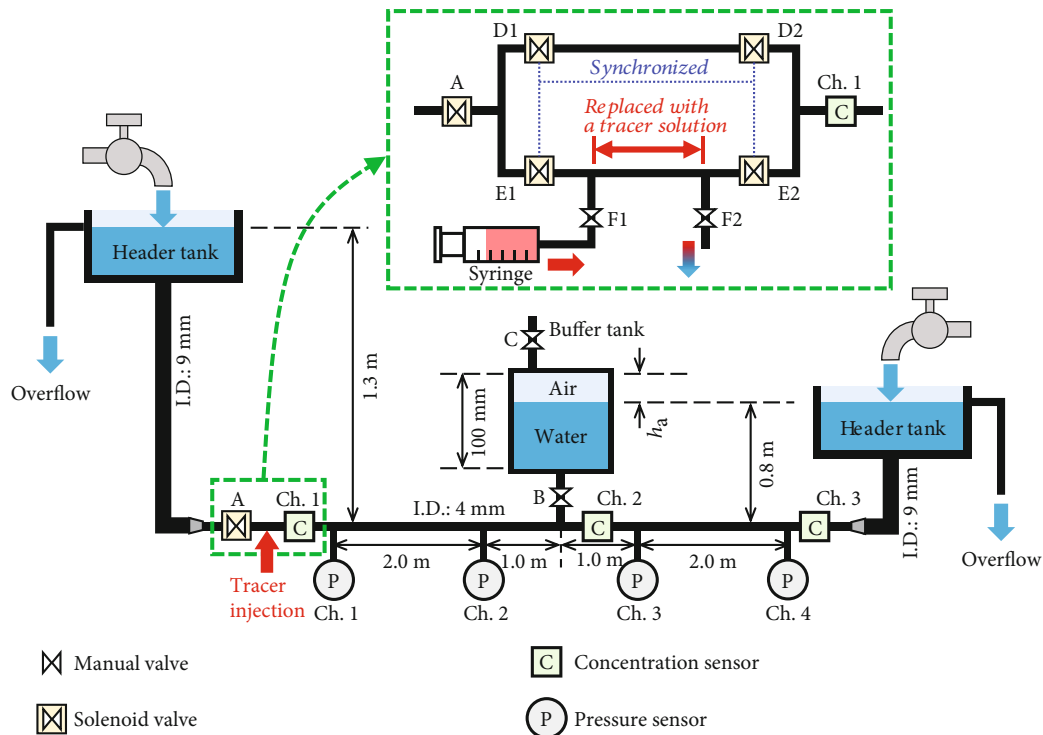
FIGURE 3: Schematic of the experimental apparatus. The detailed photos of the apparatus are provided in the Supplementary Materials.

upstream and downstream header tanks were set at 1.3 and 0.8 m, respectively, above the horizontal tube. Under a steady-state condition with this pressure gradient, the volumetric flow rate in the tube was determined in advance by measuring the overflow from the downstream header tank as 141.26 mL min^{-1} at no water supply to the downstream header tank. This value represents the average of ten measurements with a standard deviation of 1.6%. Prior to each
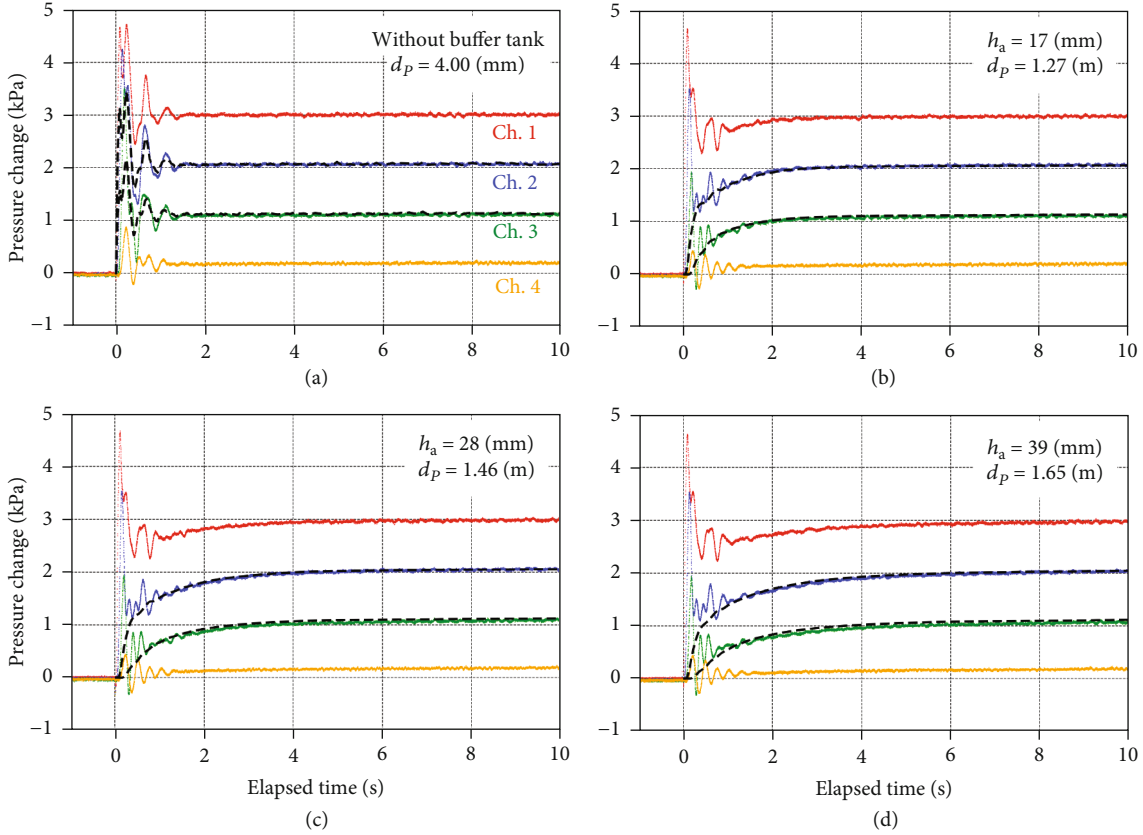
FIGURE 4: Pressure responses after opening valve A. (a) The buffer tank was disconnected. (b–d) The air thickness h_a in the buffer tank was modified from 17 to 39 mm. The colored plots indicate observations. The broken lines indicate simulations for channels 2 and 3, which refer to observations for channels 1 and 4 as boundary conditions. The apparent tube inner diameters d_P were determined to match the simulation with the observation (Table 1).

experiment, the water originally stored in the interval between valves E1 and E2 was replaced with the tracer solution (0.5 wt%).

The procedure of the experiments contained the generation and measurement of a pressure response followed by those of a tracer response. Initially, valves A, C, E1, E2, F1, and F2 were closed, whereas valves D1 and D2 were open. The state of valve B varied depending on the experiment. First, the transient pressure response upon opening valve A was measured. The pressure monitored at each sensor converged to a constant value within 10 s after valve A was opened, which indicated a steady state. After 110 s of opening valve A, the tracer was injected by closing valves D1 and D2 and simultaneously opening valves E1 and E2. The tracer response was measured for 90 s after the tracer injection. Precise time for opening and closing valves was able to be determined from pressure data that recorded noise caused by the motions of the values.

3.2. Results and Discussion.
The pressure responses during the four experiments are shown in Figure 4. All the responses initially exhibited noise with relatively high frequencies for approximately 1 s, which was caused by the motion of valve A opening. After the noise ceased, monotonous variations were observed, during which the pressure variations differed according to the buffer tank conditions.

Without the buffer tank (Figure 4(a)), the pressure response in each channel varied steeply. When the buffer tank was connected (Figures 4(b)–4(d)), the pressure responses became more gradual with increase in air thickness h_a in the buffer tank. The pressure responses for all the experiments reached a steady state, independent of the buffer tank conditions, within 10 s. The tracer responses are shown in Figure 5. All the responses exhibited a steep variation at the upstream point (channel 1), followed by gradual variations at the downstream points (channels 2 and 3) owing to mechanical dispersion. The peak concentration time in each channel implied a constant flow velocity along the horizontal tube. None of the tracer responses exhibited an apparent dependence on the buffer tank conditions.

3.2.1. Pressure Responses.
The observed pressure and tracer responses are successively investigated by following a procedure that can potentially be applied to diagnosing responses in actual fields. First, let us focus on the pressure responses associated with the volumetric flow rate. Pressure transient analysis for actual reservoirs generally includes identifying flow regimes such as radial and linear flows [23, 26]. In this study, we determined the parameters characterizing the pressure responses under a one-dimensional flow, assuming that the predominant flow regime had been identified in preceding investigations of pressure responses.
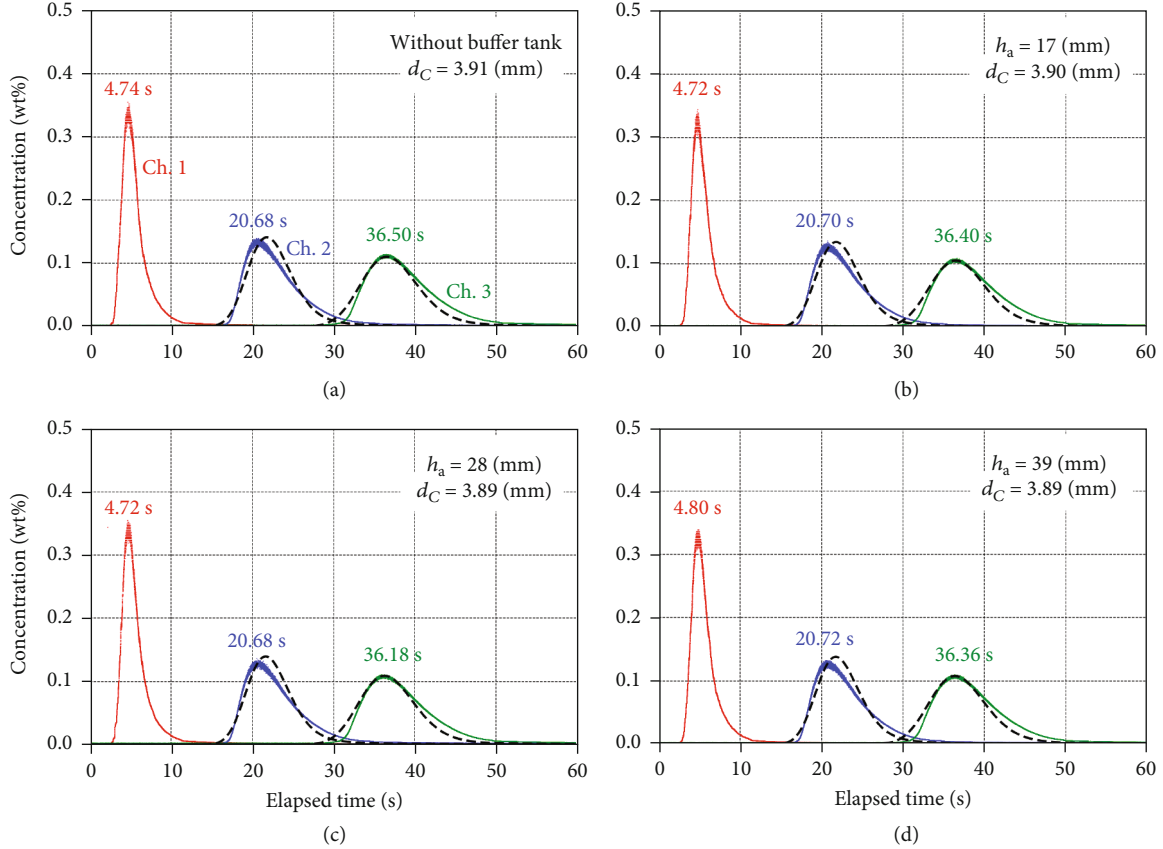
FIGURE 5: Tracer responses after tracer injection. (a) The buffer tank was disconnected. (b–d) The air thickness h_a in the buffer tank was modified from 17 to 39 mm. The colored plots indicate observations. The peak concentration time is indicated for each channel. The broken lines indicate simulations for channels 2 and 3, which refer to observation for channel 1 as an upstream boundary condition. The apparent tube inner diameters d_C were determined from the estimated flow velocity and volumetric flow rate (Table 1).

Assuming a quasi-Hagen–Poiseuille flow of water with compressibility c_w and viscosity μ in the horizontal tube with an actual inner diameter d, we obtain the following diffusion equation with respect to the pressure P, depending on time t and distance x along the tube, based on mass conservation:

$$c_w d_P^2 \frac{\partial P}{\partial t} = a \frac{d^4}{32\mu} \frac{\partial^2 P}{\partial x^2}, \tag{1}$$

where d_P and a denote the apparent inner diameter of the tube based on the pressure response and modification factor, respectively. Factors $c_w d_P^2$ and $ad^4/32\mu$ in Equation (1) correspond to the storativity and transmissivity of actual reservoirs, respectively. The apparent inner diameter d_P of the tube was allowed to vary from the actual inner diameter d depending on the buffer tank condition, as discussed below. The factor a was to modify the original Hagen–Poiseuille flow to represent the actual pressure loss due to the experimental conditions, such as the connectors and loop-shaped horizontal tube with a diameter of ~0.3 m. The factor $ad^4/32\mu$, corresponding to transmissivity, was determined based on the pressure gradient and volumetric flow rate after the steady-state condition was

reached for each experiment, assuming a quasi-Hagen–Poiseuille flow as follows:

$$a \frac{d^4}{32\mu} = -\frac{4}{\pi} \frac{Q}{dP/dx}, \tag{2}$$

where Q was the volumetric flow rate in the x-direction.

The remaining factor, $c_w d_P^2$, corresponding to storativity, was determined from the transient pressure response. Referring to the known factor $ad^4/32\mu$ and the observation for channels 1 and 4 as boundary conditions, the value of $c_w d_P^2$ was empirically determined by successively modifying and performing numerical simulations to match the numerical solution of Equation (1) with the observation for channels 2 and 3 (Figure 4). For the case without the buffer tank (Figure 4(a)), we assumed $d_P = d = 4$ (mm) as an exception. We adopted the conventional implicit finite difference method to solve Equation (1) numerically. To simulate a pressure response for 10 s, the temporal grid size expanded exponentially from 1.0×10^{-9} to 1.5×10^{-3} s, and the spatial grid size was uniform at 1.0×10^{-2} m. Thus, the parameters $c_w d_P^2$ and $ad^4/32\mu$ were successfully determined, assuming a one-dimensional flow regardless of the buffer tank condition. Referring to the compressibility c_w and viscosity μ of

TABLE 1: Parameters determined from the experiments in Section 3.

Buffer tank condition		Pressure response				Tracer response			$\frac{d_P}{d_C}$
h_a (mm)	V' * (m³)	$c_w d_P^2$ (m² Pa⁻¹)	$ad^4/32\mu$ ** (m⁴ Pa⁻¹ s⁻¹)	d_P *** (mm)	a ****	U (m s⁻¹)	D (m² s⁻¹)	d_C ** (mm)	
Disconnected		8.19×10^{-15}	6.43×10^{-9}	4.00	0.658	0.196	6.00×10^{-3}	3.91	1.02
17	1.50	8.23×10^{-10}	6.46×10^{-9}	1.27×10^3	0.660	0.197	6.00×10^{-3}	3.90	3.25×10^2
28	2.47	1.09×10^{-9}	6.45×10^{-9}	1.46×10^3	0.660	0.198	6.00×10^{-3}	3.89	3.75×10^2
39	3.44	1.40×10^{-9}	6.48×10^{-9}	1.65×10^3	0.663	0.198	6.00×10^{-3}	3.89	4.25×10^2

*Assuming an air compressibility of 6.6401×10^{-6} Pa⁻¹. **Assuming $Q = 141.26$ (mL min⁻¹). ***Assuming $c_w = 5.1210 \times 10^{-10}$ (Pa⁻¹) at the ambient pressure (996.9 hPa) and temperature (28.8°C). ****Assuming $d = 4$ (mm) and $\mu = 8.1823 \times 10^{-4}$ (Pa s) at the ambient pressure and temperature.

water as well as the actual inner diameter d, we determined the apparent inner diameter d_P and modification factor a (Table 1). The equation of state IAPWS-IF97 and an empirical equation developed by the International Association for the Properties of Water and Steam (IAPWS) [72, 73] were employed to compute c_w and μ.

3.2.2. Tracer Responses. The tracer responses associated with the volumetric flow rate are subsequently investigated based on a one-dimensional flow, which is assumed to be identified by analyzing the pressure responses in advance. We obtain the advection–dispersion equation with respect to the tracer concentration C in the horizontal tube as follows:

$$\frac{\partial C}{\partial t} + U \frac{\partial C}{\partial x} = D \frac{\partial^2 C}{\partial x^2}, \tag{3}$$

where U and D are flow velocity and dispersion coefficient, respectively. The flow velocity U was determined from the travel time (i.e., peak concentration time) (Figure 5) at each concentration sensor using linear regression. The apparent inner diameter of the tube d_C based on the tracer response was subsequently determined using the relationship with the volumetric flow rate $\pi d_C^2 U = 4Q$. Referring to the known factor U and observation for channel 1 as the upstream boundary condition, the value of D was empirically determined by successively modifying and performing numerical simulations to match the numerical solution of Equation (3) with the observation for channels 2 and 3 (Figure 5). An outflow boundary was assumed for the downstream boundary condition at the sensor for channel 3. We adopted the constrained interpolation profile method [74, 75] to overcome numerical dispersion when numerically solving the advection term, whereas the conventional explicit finite difference method was applied to the dispersion term. The grid sizes for temporal and spatial discretization were 1.0×10^{-4} s and 1.0×10^{-2} m, respectively.

The parameters determined from the pressure and tracer responses associated with the volumetric flow rate are summarized in Table 1. Remarkably, the responses were successfully simulated by assuming a one-dimensional flow regardless of the buffer tank condition. The apparent inner diameter d_P, depending on the equivalent volume V' of the water-filled buffer tank (Appendix A), tends to have an unrealistically large value, whereas d_C appears to be approx-imately constant and comparable with the actual value (4 mm). The pressure and tracer responses individually yield apparent inner diameters d_P and d_C, or apparent cross-sectional areas in general, reflecting the total hydraulic volume and partial volume swept by the tracer, respectively. The difference between the apparent diameters indicates the existence of dead-end features that restricts the swept volume.

4. Numerical Simulations

4.1. Methods. The concept described in Section 2 is numerically validated using reservoir models associated with unknown dead-end features. The dead-end features are generated by deep unknown permeable layers parallel to a shallow known layer. We investigate the pressure and tracer responses while injecting using a well by determining the apparent parameters, assuming only the known layer, to characterize the responses. The pressure and tracer responses were simulated using the code presented by Matsumoto [76]. This code was designed by focusing on pressure and tracer responses while producing and/or injecting in particular, compared with the multipurpose simulators for geothermal systems such as TOUGH2 [77], TOUGH3 [78], and Waiwera [79]. A single-phase and nonisothermal discrete fracture network model, based on the finite difference method, was adopted to depict reservoirs consisting of planar permeable structures. Using this code, a highly refined local grid enables to simulate pressure responses in a flowing well by accurately reproducing the steep pressure variations in the vicinity of the wellbore. The accuracy of tracer responses is conserved using the constrained interpolation profile method [74, 75], which effectively reduces numerical dispersion. The thermodynamic properties and viscosity of water obey the empirical equations developed by IAPWS [72, 73]. A one-dimensional radial flow along only the known layer, obeying the analytical solutions [19, 80], was assumed to characterize the pressure and tracer responses simulated numerically.

Reservoir models containing a known horizontal layer and different numbers of unknown layers are illustrated in Figure 6. Assuming an extremely large dimension of 2000 km for the known square layer, we intended to place an infinite-acting external boundary. We assumed square unknown layers with a common dimension of 12 km placed at a regular spacing of 400 m below the known layer. The

unknown layers were bordered by impermeable boundaries to generate dead-end features. All layers were intersected by an unknown vertical fault with negligible displacement. A reinjection well penetrated only the known layer at an intersection 1000 km from each side. A monitoring well intersecting only the known layer was located 1 km from the reinjection well, which was assumed to be producing at a negligible flow rate to monitor the tracer concentration. The unknown fault passed through the midpoint between the reinjection and monitoring wells.

In the natural state, the reservoir pressure followed a hydrostatic pressure distribution of 10 MPa at a depth of the known layer. The specific enthalpy was uniform at 600 kJ kg^{-1} (i.e., approximately uniform temperature distribution at 141°C). The permeability–thickness product, porosity–thickness product, and dispersion coefficient for the tracer were uniform and constant at 1.0×10^{-11} m^3, 1.0×10^{-1} m, and 1.0×10^{-2} m^2 s^{-1}, respectively. The injection rate was maintained at 200 t h^{-1} for 300 d. The specific enthalpy of the injected fluid was identical to that of the fluid originally stored in the reservoir, implying isenthalpic conditions. Subsequently, an inert tracer was mixed with the injected fluid 100–101 d after starting injection. The tracer concentration of the injected fluid was maintained at 10 ppm.

A two-dimensional Cartesian numerical grid was defined for each planar permeable structure parallel to its sides. The grid size of the known layer in both directions was uniform at 100 m, within 3 km from the reinjection well. In the outer region, the grid size expanded exponentially from 100 m to 250 km. The total number of grid points in each direction was 121. The unknown layers had the same grid as the known layers. To limit the effective dimension of the unknown layers to 12 km, as defined above, an impermeable region was defined, except for the valid region, within 6 km from the projection point of the reinjection well onto each unknown layer. The planar structure representing the unknown fault had the same grid and impermeable region in the strike direction as the unknown layers, whereas the grid size in the vertical direction is uniform at 100 m. The temporal grid size expanded exponentially from 0.159 s after 3 d since starting injection, followed by a constant value of 1.32 h.

4.2. Results and Discussion

4.2.1. Pressure Responses. The simulated pressure and tracer responses are successively investigated following a procedure similar to that in Section 3, which is potentially applicable to diagnosing the responses in actual fields. First, we focus on the pressure responses associated with the volumetric flow rate to determine the porosity–thickness and permeability–thickness products, as well as the storativity and transmissivity, using the conventional semilog analysis. We characterize the pressure responses by assuming only the known layer, regardless of the actual permeable structures including the unknown layers and fault. The semilog plot of the pressure responses at the monitoring well is shown in Figures 7(a) and 7(b). The pressure variations for all models, assuming different numbers of unknown layers, converged to straight
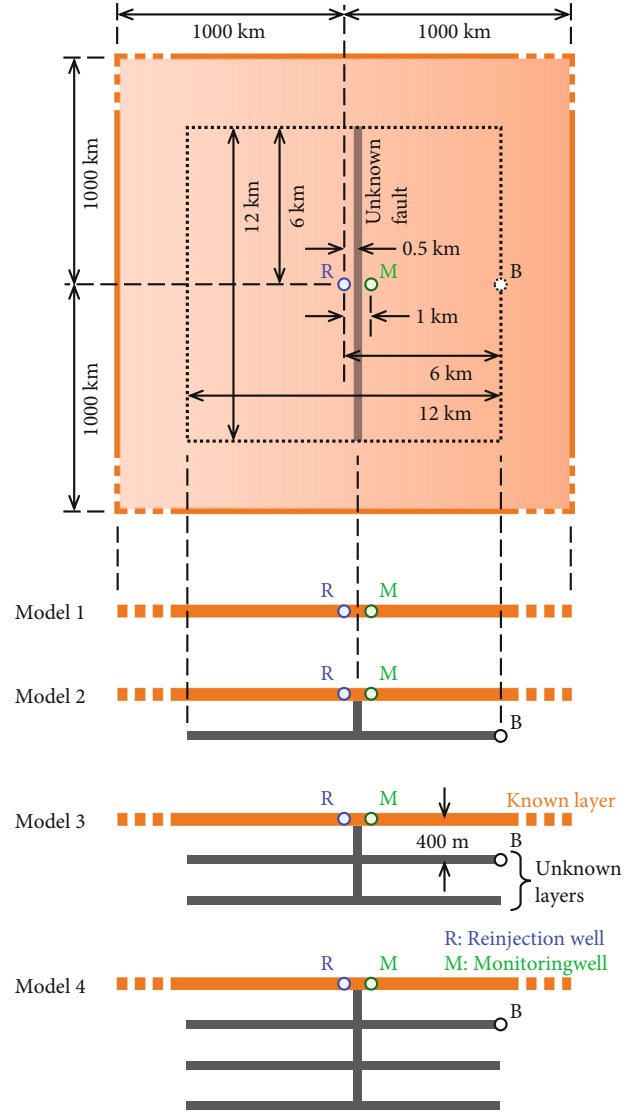
FIGURE 6: Orthographic projections of the reservoir models with different numbers of unknown layers. Model 1 assumes only the known layer. Models 2–4 assume one to three unknown layers, respectively, connected through the unknown fault with a regular spacing. Point B is at the impermeable boundary of the uppermost unknown layer.

lines with an approximately common slope and different intercepts. Interpreting these straight lines based on the conventional line-source solution [19], which assumed only the known layer, the storativity $c_w \langle \phi h \rangle_P$ and transmissivity kh/μ were determined as summarized in Table 2, where ϕ, h, and k were the porosity, thickness, and permeability of the layer storing water with compressibility c_w and viscosity μ. The bracketed and scripted porosity–thickness product $\langle \phi h \rangle_P$ denotes that it was determined from the pressure responses. The natural-state pressure and specific enthalpy of the known layer were referenced to determine the volumetric flow rate Q for injection and, eventually, the porosity–thickness product $\langle \phi h \rangle_P$ and permeability–thickness product kh (Table 2).
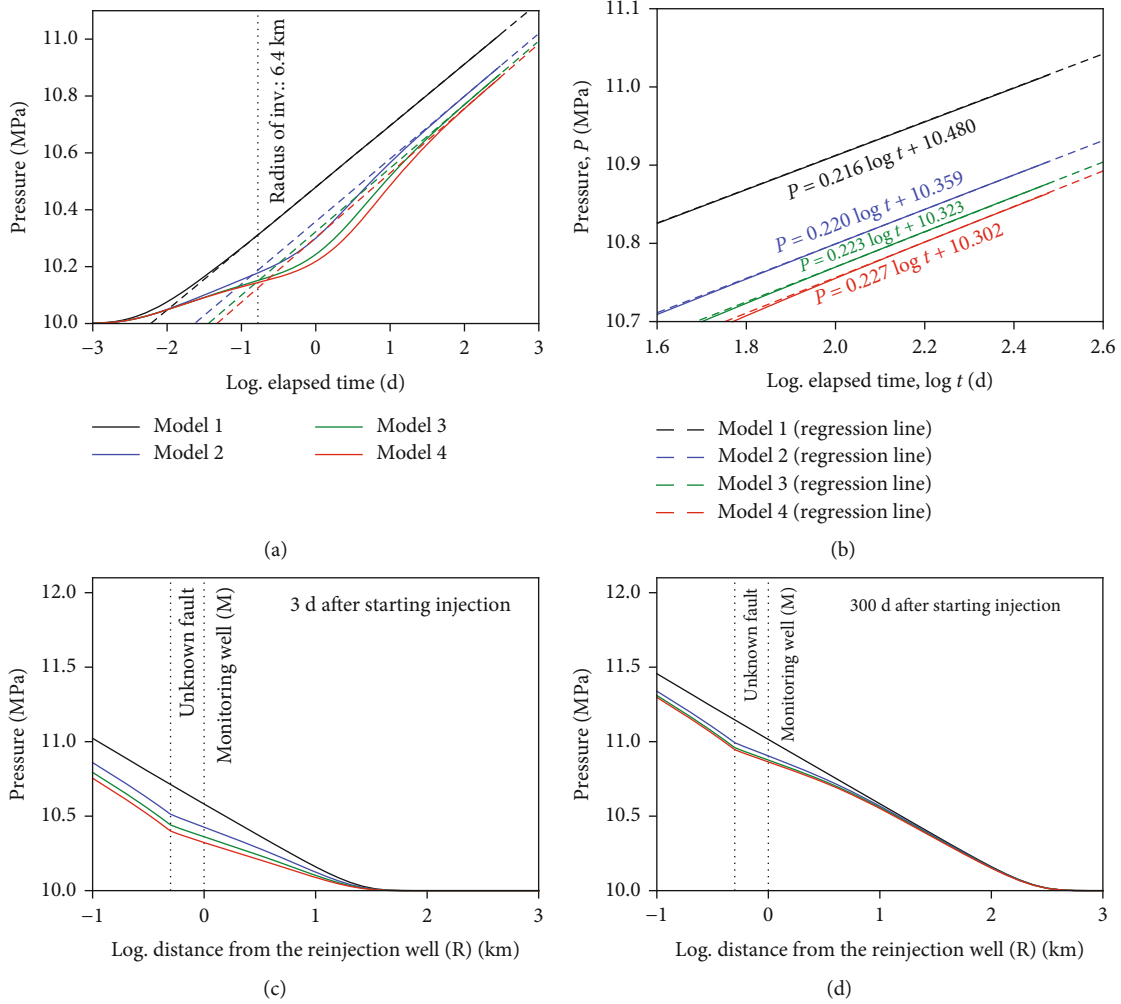
FIGURE 7: (a, b) Pressure responses at the monitoring well (M) on different scales and (c, d) pressure distributions along the known layer from the reinjection well (R) through the unknown fault and monitoring well after 3 and 300 d for models 1–4 (Figure 6). At the time indicated by the (a) dotted line, the radius of investigation reached point B, 6.4 km from the reinjection well. The broken regression straight lines were determined referring to (a, b) pressure variations after 100 to 300 d.

TABLE 2: Parameters determined by analyzing the simulated responses in Section 4.

Model	Number of unknown layers	Pressure response				Tracer response			$\frac{\langle\phi h\rangle_P}{\langle\phi h\rangle_C}$
		$c_w\langle\phi h\rangle_P{}^*$ (m Pa^{-1})	kh/μ^* (m^3 Pa^{-1} s^{-1})	$\langle\phi h\rangle_P{}^{**}$ (m)	kh^{***} (m^3)	Δt (d)	$\langle\phi h\rangle_C{}^{*,****}$ (m)	
1	0	5.95×10^{-11}	5.06×10^{-8}	0.0836	9.99×10^{-12}	48.9	0.0804	1.04
2	1	2.26×10^{-10}	4.97×10^{-8}	0.317	9.81×10^{-12}	55.8	0.0916	3.46
3	2	3.40×10^{-10}	4.90×10^{-8}	0.478	9.67×10^{-12}	56.4	0.0927	5.15
4	3	4.39×10^{-10}	4.82×10^{-8}	0.617	9.51×10^{-12}	56.7	0.0932	6.62

*Assuming $Q = 5.97\times10^{-2}$ (m^3 s^{-1}) at the reservoir pressure (10 MPa) and specific enthalpy (600 kJ/kg). **Assuming $c_w = 7.1132\times10^{-10}$ (Pa^{-1}) at the reservoir pressure and specific enthalpy. ***Assuming $\mu = 1.9738\times10^{-4}$ (Pa s) at the reservoir pressure and specific enthalpy. ****Assuming $r_w = 8.5/2$ (inch).

The different intercepts among the straight lines of the pressure responses were due to delay in pressure increase during an early period, depending on the unknown layers and fault. The dotted line in Figure 7(a) indicates the time t when a radius of investigation $2\sqrt{(kh/\mu)/(c_w\phi h)\cdot t}$ [81] reached the closest point at the impermeable boundary of the uppermost unknown layer (point B) 6.4 km from the reinjection well (point R) (Figure 6). This radius of investigation is based on the permeability–thickness and porosity–thickness products of 1.0×10^{-11} m^3 and 1.0×10^{-1} m, respectively, as assumed for the simulations, under the reservoir pressure of 10 MPa and specific enthalpy of 600 kJ. Before the radius of investigation reached point B, the pressure responses exhibited different slopes depending on the

(a)

(b)

(c)

(d)
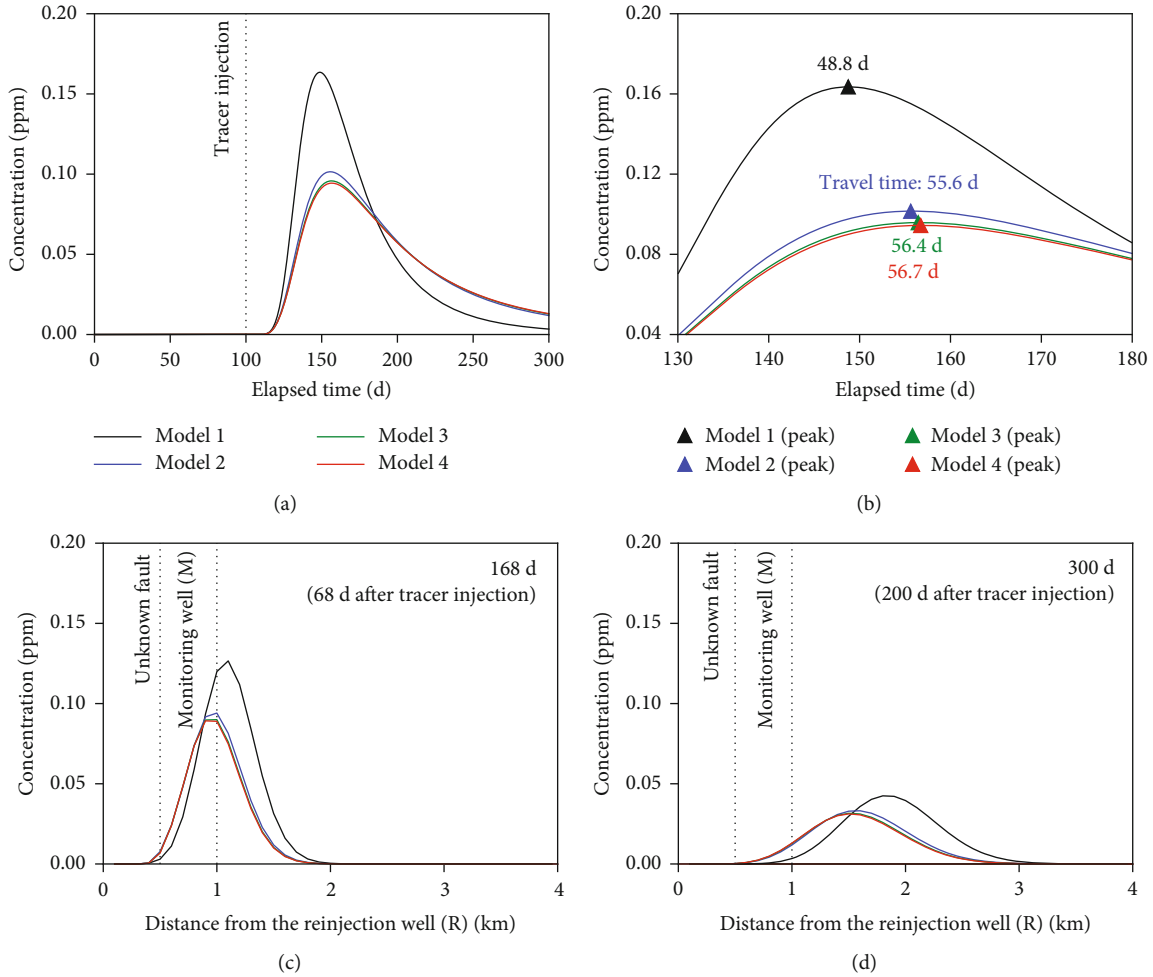
FIGURE 8: (a, b) Tracer responses at the monitoring well (M) on different scales and (c, d) tracer concentration distributions along the known layer from the reinjection well (R) through the unknown fault and monitoring well after 168 and 300 d (68 and 200 d after tracer injection) for models 1–4 (Figure 6). The tracer was mixed into the injected fluid after 100 to 101 d since (a) starting injection. The travel time was estimated from the (b) peak concentration time.

unknown layers and fault, implying responses from multiple infinite-acting layers (Figure 7(a)). The pressure responses eventually converged to straight lines with a common slope, successively affected by the impermeable boundaries of the unknown layers. As such, the apparent porosity–thickness products $\langle\phi h\rangle_P$, assuming only the known layer, depended on the existence of the unknown layers and fault (Table 2).

The pressure distributions along the known layer from the reinjection well (point R) through the unknown fault and monitoring well (point M) (Figure 6) are shown in Figures 7(c) and 7(d) on a logarithmic scale. The pressure distributions for models 2–4 exhibited a bend at the unknown fault owing to fluid flow toward the unknown layers, whereas model 1, without unknown layers, exhibited a typical straight line with a common slope obeying the analytical solution [19]. This outflow yielded the increase in the apparent porosity–thickness products $\langle\phi h\rangle_P$ through the delay in pressure increase at the monitoring well (Figures 7(a) and 7(b)). At each distance from the reinjection well, pressure differences among the models will con-

verge to constant values as implied by the temporal variations at the monitoring well, unless the fronts of the pressure variations reach the outer boundary of the known layer 1000 km from the reinjection well.

4.2.2. Tracer Responses. Subsequently, we investigate the tracer responses at the monitoring well (Figures 8(a) and 8(b)) associated with the volumetric flow rate by assuming only the known layer. We assume that a one-dimensional quasi-steady-state radial flow originating in the reinjection well has been identified by analyzing the pressure responses as well as, in an actual field, several geoscientific surveys that successfully identified the known layer. In an incompressible radial flow, the velocity of a fluid element is inversely proportional to the distance r from the source to satisfy mass conservation, as follows [80]:

$$\frac{dr}{d\Delta t} = \frac{Q}{2\pi\langle\phi h\rangle_C}\frac{1}{r}, \tag{4}$$
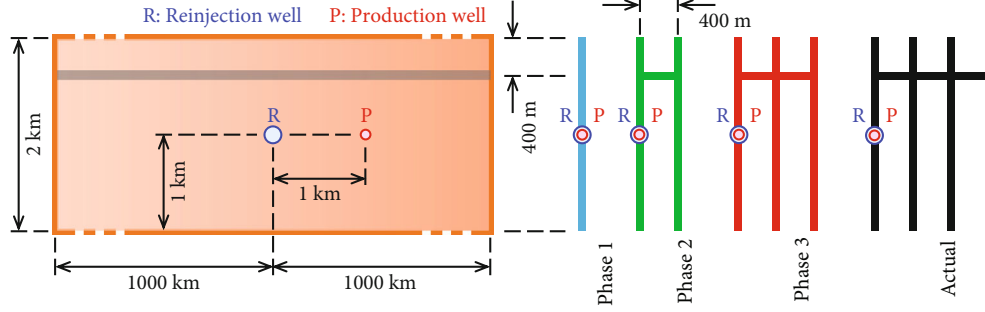
FIGURE 9: Orthographic projections of the reservoir models with different numbers of vertical faults. The model with four faults is assumed to be accurately representing the actual reservoir. The model at each phase of the hypothetical exploration only assumes currently identified faults.

where Δt, Q, and $\langle \phi h \rangle_C$ are travel time, volumetric flow rate for injection, and porosity–thickness product determined from the tracer responses, respectively. Assuming that the distance r at $\Delta t = 0$ is equal to the wellbore radius r_w, we obtain the porosity–thickness product depending on the travel time Δt to reach a distance r as follows:

$$\langle \phi h \rangle_C = \frac{Q}{\pi} \frac{\Delta t}{r^2 - r_w^2}. \quad (5)$$

We determined the porosity–thickness product $\langle \phi h \rangle_C$ for each model based on the travel time estimated from the peak concentration time at the monitoring well (Figure 8(b)).

The parameters determined from the pressure and tracer responses associated with the volumetric flow rate are summarized in Table 2. The responses were successfully characterized by assuming only the known layer, regardless of the unknown layers and fault. The apparent porosity–thickness product $\langle \phi h \rangle_P$ based on the pressure responses increases with an increase in the number of unknown layers, whereas $\langle \phi h \rangle_C$ based on the tracer responses is poorly variable and comparable with the actual value of the known layer (0.1 m). The tracer responses involving outflow toward the unknown layers (models 2–4) became more gradual than that of model 1, without the unknown layer, owing to slightly smaller flow velocities (Figures 8(a) and 8(d)). Nevertheless, the apparent porosity–thickness products $\langle \phi h \rangle_C$ estimated from the peak concentration time were free from severe degradation. As discussed regarding the experimental results in Section 3, the apparent porosity–thickness products $\langle \phi h \rangle_P$ and $\langle \phi h \rangle_C$ reflect the total hydraulic volume and partial volume swept by the tracer, respectively, which potentially provides a useful perspective for characterizing the existence of unknown dead-end features in actual fields.

5. Potential Application to Hypothetical Exploration

5.1. Methods. Herein, we demonstrate the potential application of the concept validated above to hypothetical exploration consisting of multiple phases, which includes geoscientific surveys, exploration drilling, and well testing [24]. Let us assume a reservoir at a prospect consisting of four parallel-distributed vertical faults, connected to each other hydraulically. Three phases of exploration identify the faults individually, which yields a reservoir model successively updated with the progress of the exploration. We investigate the evolution of the apparent porosity–thickness products determined using the up-to-date reservoir model at each phase, which potentially depicts the improvement of the reservoir model. The pressure and tracer responses were simulated using the same code [76] as that adopted in the numerical simulations of Section 4. Defining the pressure-buffering pores, Matsumoto [76] theoretically derived and applied a mathematical model involving the extended and conventional porosities, which equivalently corresponded to the apparent porosity–thickness products generated by dead-end features discussed in this study. We adopted this mathematical model to simulate the pressure and tracer responses, depending on the apparent porosity–thickness products $\langle \phi h \rangle_P$ and $\langle \phi h \rangle_C$, respectively.

The reservoir model assumed at each phase of the hypothetical exploration, as well as that accurately representing the actual reservoir, is depicted in Figure 9. The vertical faults, connected through a horizontal permeable structure, had common dimensions of 2 and 2000 km in the vertical and horizontal directions, respectively. Assuming an extremely large horizontal dimension for both the vertical faults and horizontal permeable structure, we intended to place infinite-acting boundaries. The top and bottom boundaries of each fault were impermeable. The spacing between the faults was uniform at 400 m, and all faults were connected 400 m from the upper boundary. The production and reinjection wells intersected one of the faults at the vertical middle points with a spacing interval of 1 km.

Under a natural state, the reservoir pressure followed a hydrostatic pressure distribution of 12 MPa 400 m from the top boundary. The specific enthalpy was uniform at 900 kJ kg^{-1} (i.e., approximately uniform temperature at 210°C). The production and reinjection rates were constant at 200 and 160 t h^{-1}, respectively. The specific enthalpy of the reinjected fluid was the same as that of the fluid originally stored in the reservoir, implying isenthalpic conditions. Subsequently, an inert tracer was injected into the reinjected fluid 100–101 d after starting production and reinjection. The tracer concentration of the reinjected fluid was

maintained at 10 ppm. For the model representing the actual reservoir, the permeability–thickness product, porosity–thickness product, and dispersion coefficient for the tracer were uniform and constant at $1.0 \times 10^{-11}\,\mathrm{m}^3$, $1.0 \times 10^{-1}\,\mathrm{m}$, and $1.0 \times 10^{-2}\,\mathrm{m}^2\,\mathrm{s}^{-1}$, respectively. For the other model assumed at each phase, the values of these parameters were empirically determined by successively modifying to match the simulated pressure and tracer responses with the synthetic observations, generated by the model representing the actual reservoir.

A two-dimensional Cartesian numerical grid was defined for each fault and the horizontal permeable structure. The grid size of the vertical faults in the vertical direction was uniform at 100 m, whereas that in the horizontal direction varied depending on the region. In the inner region (3 km from the reinjection well toward both sides), the grid size was uniform at 100 m. In the outer regions, the grid size expanded exponentially from 100 m to 250 km. The grid size of the horizontal permeable structure was 100 m, perpendicular to the vertical faults. In the direction parallel to the vertical faults, the grid size was identical to that of the vertical faults. To accurately simulate the pressure variations at the production well, we applied a highly refined local grid with a size down to 1 mm around the 8.5-inch wellbore. The temporal grid size expanded exponentially from $1.91 \times 10^{-7}\,\mathrm{s}$ after 3 d since starting production and reinjection, followed by a constant value of 1.49 h.

5.2. Results and Discussion

5.2.1. Calibration of Reservoir Models.
First, we obtained the synthetic observations by simulating the pressure and tracer responses using the model representing the actual reservoir with four vertical faults. The reservoir model assumed at each phase of the hypothetical exploration was subsequently calibrated to reproduce the synthetic observations. We first matched the pressure response by allowing the permeability–thickness product kh and porosity–thickness product $\langle \phi h \rangle_P$ to be modified, followed by matching the tracer response. When matching the tracer response by allowing the porosity–thickness product $\langle \phi h \rangle_C$ and dispersion coefficient D to be modified, we particularly allowed $\langle \phi h \rangle_C$ to have a different value from $\langle \phi h \rangle_P$. Thus, the calibration followed a straightforward procedure without being back to matching the pressure response because the modification of $\langle \phi h \rangle_C$ and D while matching the tracer response did not affect the pressure response.

The pressure and tracer responses from the successfully calibrated reservoir model at each phase are superimposed on the synthetic observations in Figure 10. The colored broken lines in Figures 10(b1)–10(b3), inaccurately reproducing the synthetic observation, denote the tracer responses simulated using the porosity–thickness products determined from the pressure responses (i.e., assuming $\langle \phi h \rangle_C = \langle \phi h \rangle_P$). These results imply that assuming different porosity–thickness products for the pressure and tracer responses is essential for successfully reproducing the synthetic observations. The distributions of tracer concentration along the fault

intersected by the production and reinjection wells are shown in Figure 11 for each reservoir model. The flow of the tracer obeyed the velocity field generated by the production and reinjection. Except for phase 1, the distributions were asymmetric owing to flow through the horizontal permeable structure intersected 400 m from the top. The fluid in the reservoir for all models did not flash throughout the simulation period of 300 d.

The assumed and determined parameters of the reservoir models are listed in Table 3. The permeability–thickness product kh did not need to be modified to reproduce the synthetic observations using the model assumed at each phase, resulting in a common value. The dispersion coefficient D of the model for phase 1, assuming a single fault, required a relatively large value, which potentially compensated for the absence of flow through the horizontal permeable structure. As the exploration progressed, both the apparent porosity–thickness products $\langle \phi h \rangle_P$ and $\langle \phi h \rangle_C$ determined from the pressure and tracer responses, respectively, approached the actual value of 0.1. The distribution of tracer concentration also approached that of the actual reservoir (Figure 11).

As seen in conventional well test analysis [23], the pressure responses can be interpreted as a superposition of those for two problems: production and reinjection at the same rate of $160\,\mathrm{t\,h}^{-1}$ and production at a rate of $40\,\mathrm{t\,h}^{-1}$ without reinjection. The pressure-response component obeying the former problem converges to a steady state that depends solely on transmissivity kh/μ. In contrast, the latter problem represents production that generates a linear flow depending solely on the product of transmissivity kh/μ and storativity $c_{\mathrm{w}}\langle \phi h \rangle_P$ [31]. By combining these two problems, we can ensure that the pressure responses rely independently on kh and $\langle \phi h \rangle_P$ when the viscosity μ and compressibility c_{w} are assumed, as in this study.

5.2.2. Implication of Apparent Porosity–Thickness Products.
The evolution of the apparent porosity–thickness products $\langle \phi h \rangle_P$ and $\langle \phi h \rangle_C$ with the progress of the hypothetical exploration is depicted using a logarithmic ratio in Figure 12. Owing to $\langle \phi h \rangle_P$ and $\langle \phi h \rangle_C$, indicating the total hydraulic volume and partial volume swept by the tracer, respectively, $\log\left(\langle \phi h \rangle_P / \langle \phi h \rangle_C\right)$ at each phase had a positive value and approached zero, indicating the actual reservoir. This evolution depicts the successive improvement of the reservoir model to accurately reproduce the actual reservoir, which will provide strategic guides for successful exploration and development in actual fields. Extremely large porosity–thickness products (e.g., tens of meters or more) or equivalent storativities based on pressure responses, as in this study, were reported in actual fields [25, 82, 83], which remain unstudied by quantitatively characterizing and/or systematically validating. The comparison between the porosity–thickness products $\langle \phi h \rangle_P$ and $\langle \phi h \rangle_C$ will provide an insightful scale to characterize this problem, potentially indicating the deviation of permeable structure between a reservoir model and an actual reservoir. Future studies will attempt to determine the evolution of $\langle \phi h \rangle_P$ and $\langle \phi h \rangle_C$ in actual
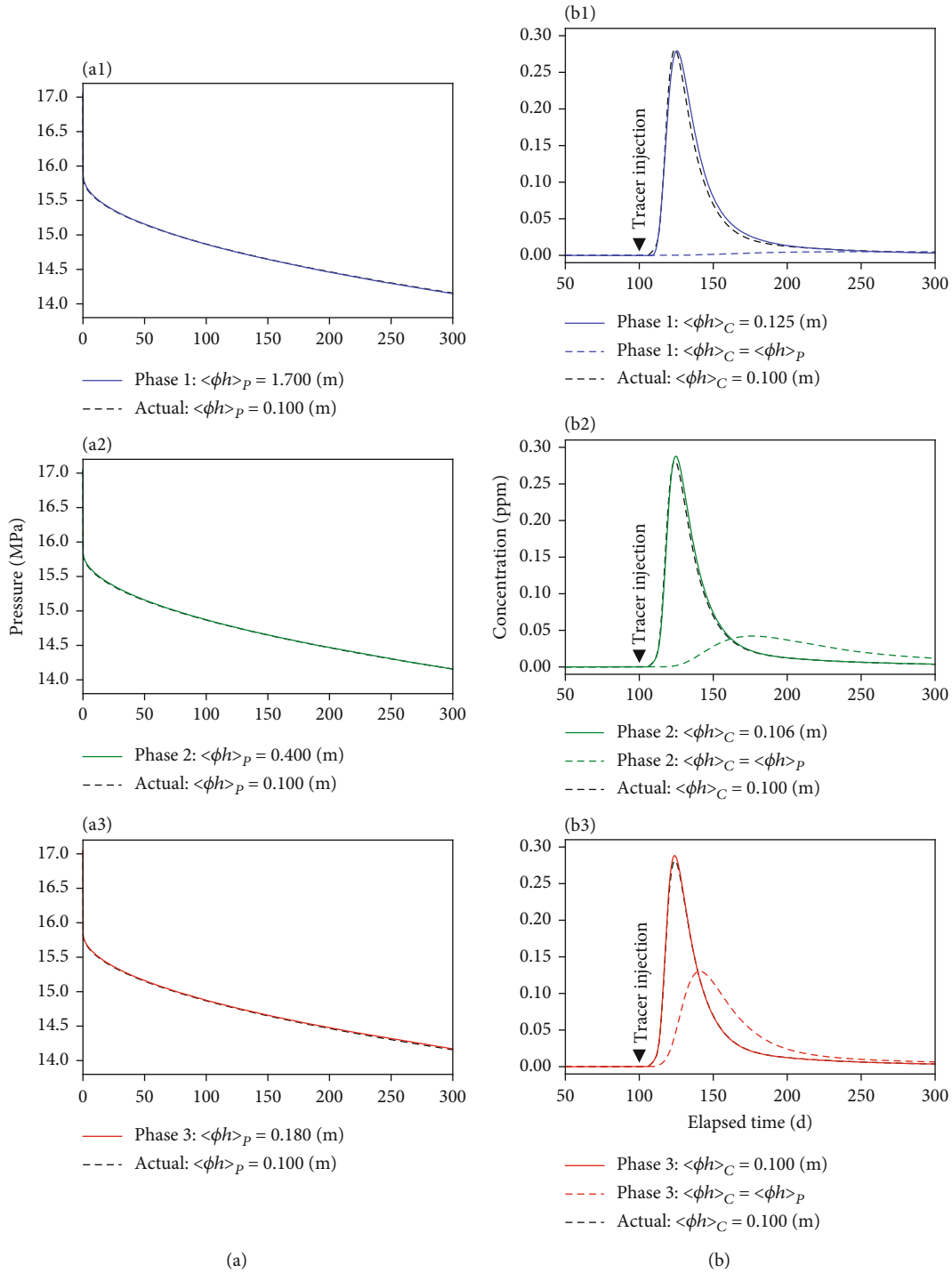
FIGURE 10: Pressure and tracer responses at the production well. The (a1–a3) pressure and (b1–b3) tracer responses simulated using the reservoir model assumed at each phase (solid lines) successfully reproduced the synthetic observations (dotted lines), generated by the model representing the actual reservoir (Figure 9). The colored broken lines denote the tracer responses simulated using the porosity–thickness products determined from the pressure responses (i.e., assuming $\langle \phi h \rangle_C = \langle \phi h \rangle_P$).

fields for further validation of this concept. We will particularly focus on investigating the typical range of $\log\left(\langle \phi h \rangle_P / \langle \phi h \rangle_C\right)$ at each stage of exploration and development at the prospects of geothermal and, potentially, general geofluid resources.

Assuming kh and $\langle \phi h \rangle_C$ for each planar permeable structure in a reservoir model, which are poorly dependent of dead-end features (Table 3), we can potentially determine a possible distribution of the permeable structures by modifying the model to reproduce observed pressure and tracer
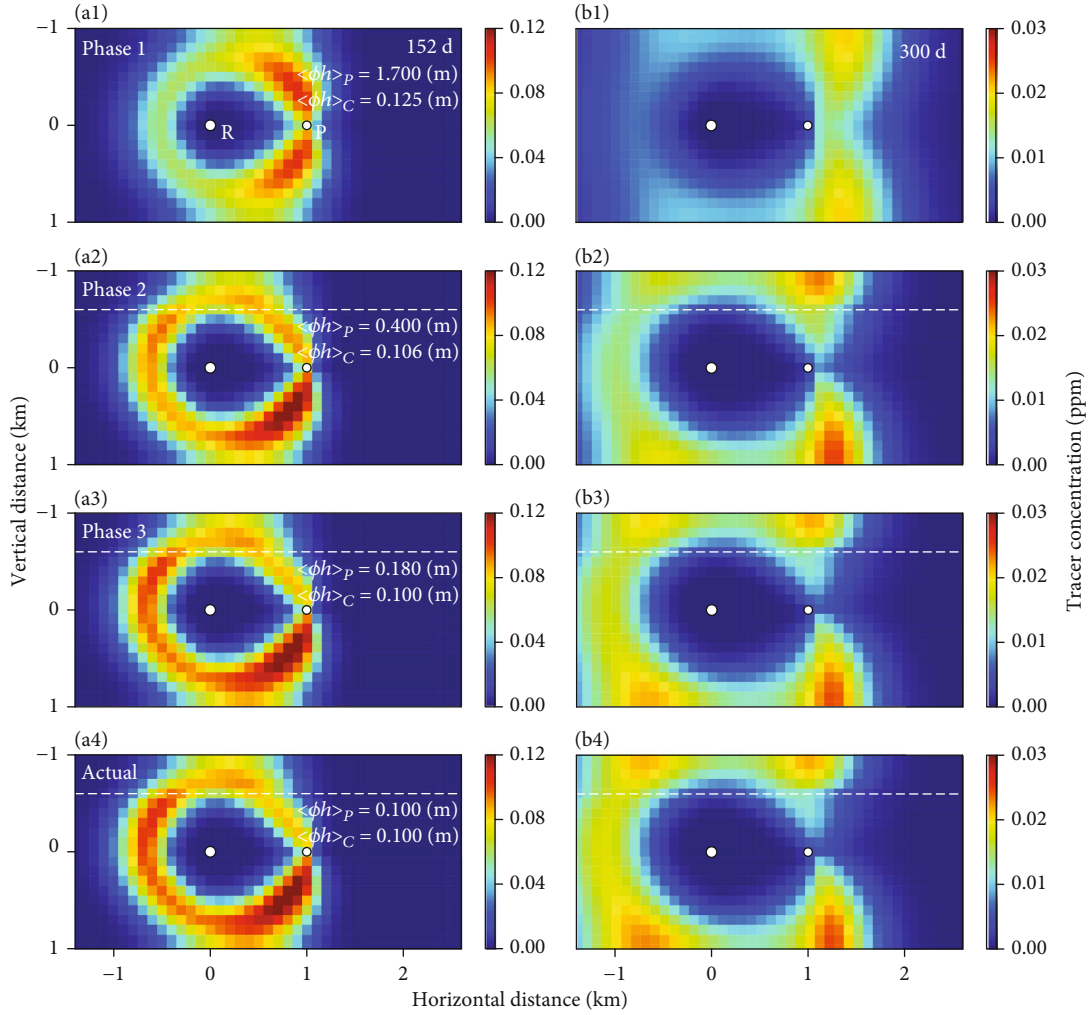
FIGURE 11: Distributions of the tracer concentration along the fault (Figure 9) intersected by the production (P) and reinjection (R) wells (a1–a4) 152 and (b1–b4) 300 d after starting production and reinjection. The dotted lines denote the intersection of the fault and horizontal permeable structure, connecting multiple faults.

TABLE 3: Parameters for the simulations in Section 5.

Model	Pressure response		Tracer response		$\frac{\langle \phi h \rangle_P}{\langle \phi h \rangle_C}$
	$\langle \phi h \rangle_P$ (m)	kh (m³)	D (m² s⁻¹)	$\langle \phi h \rangle_C$ (m)	
Phase 1	1.700**	1.00×10^{-11}**	1.35×10^{-2}**	0.125**	13.6
Phase 2	0.400**	1.00×10^{-11}**	1.00×10^{-2}**	0.106**	3.77
Phase 3	0.180**	1.00×10^{-11}**	1.00×10^{-2}**	0.100**	1.80
Actual	0.100*	1.00×10^{-11}*	1.00×10^{-2}*	0.100*	1.00

*Assumed values. **Determined to successfully reproduce the synthetic observations.

responses in an actual field while satisfying $\langle \phi h \rangle_P = \langle \phi h \rangle_C$. This possible distribution will be considerably constrained by referring to subsurface images obtained from geophysical surveys to be interpreted as in Figure 2. Even though the state-of-the-art techniques of geophysical surveys successfully image the multidimensional distributions of physical parameters (e.g., density, electrical resistivity, and seismic velocities) reflecting geological structure [84–87], the direct

identification of open fractures, which may or may not be associated with discontinuous features in the distributions, is still challenging. Future studies will combine the concept of this study with geophysical surveys to improve the effectiveness of exploration. The combined technique will yield significant cost efficiency because the concept of this study only requires the readily available data of conventional pressure transient and tracer tests, performed frequently.
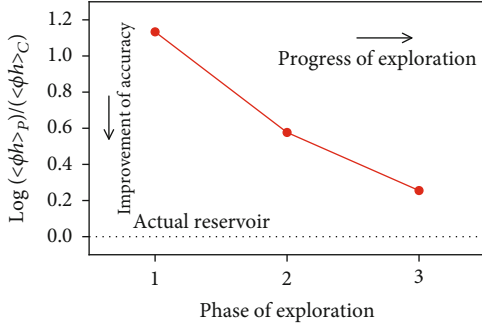
FIGURE 12: Evolution of the apparent porosity–thickness products $\langle\phi h\rangle_P$ and $\langle\phi h\rangle_C$ based on pressure and tracer responses, respectively, with the progress of hypothetical exploration. The logarithmic ratio of the apparent porosity–thickness products potentially indicates the accuracy of the up-to-date reservoir model at each phase.
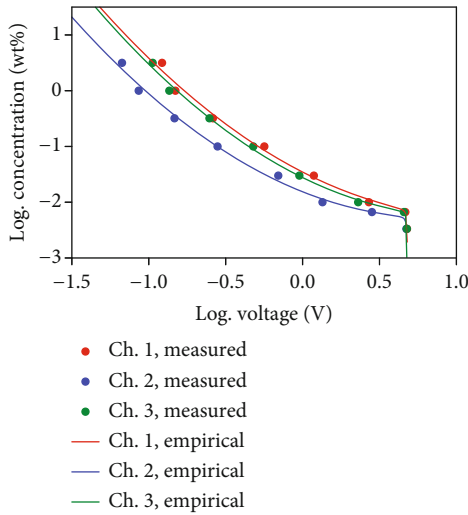
FIGURE 13: Relationship between tracer concentration and output voltage for each concentration sensor. The empirical relationships obey Equation (A.1) with the constants summarized in Table 4.

To successfully apply the concept of this study, several limitations and further practical conditions must be considered, which remain unstudied. Accurately estimated total compressibility is essential for determining the apparent porosity–thickness product from storativity: storativity is defined as the product of total compressibility and porosity–thickness product. The total compressibility potentially varies by orders of magnitude owing to boiling and the existence of unconfined aquifers [25, 83]. The impact of thermo-hydro-mechanical processes in fractured rocks [1, 88, 89] remains unstudied. To successfully identify and/or predict such effects, comprehensive understanding of a hydrothermal system from diverse perspectives of geosciences, including geology, hydrology, geophysics, and geochemistry, is essential as in currently standard exploration and development [24]. Tracer responses also need to be accurately interpreted through an adequate understanding of several effects, such as adsorption and decomposition

TABLE 4: Empirical constants for Equation (A.1).

n	a_n	b_n	c_n	d_n	$\log E_{0n}$ (V)
1	−1.45790	−1.40794	0.634143	0.00105583	0.681784
2	−1.81174	−1.09609	0.661727	0.000914718	0.678973
3	−1.55684	−1.35305	0.679273	0.000940129	0.680879

of tracers, as well as background natural flow through a reservoir [48]. In particular, flow paths along a fracture surface are potentially restricted owing to nonuniform aperture distribution [60, 61], which will be also taken into account in future studies.

6. Conclusions

We have presented and validated a novel perspective for improving the understanding of permeable structures at geothermal prospects by jointly diagnosing the responses of pressure transient and tracer testing. The pressure and tracer responses individually yield apparent porosity–thickness products, reflecting the total hydraulic volume and partial volume swept by a tracer, respectively. The difference between these apparent porosity–thickness products implies the existence of unknown dead-end features involved in a reservoir model, reproducing the observation of pressure and tracer responses.

This concept has been validated through laboratory experiments and numerical simulations, generating pressure and tracer responses. The laboratory experiments using a quasi-Hagen–Poiseuille flow through a tube, connected to a buffer tank, individually yielded apparent inner diameters. The numerical simulations assuming a known layer, connected to unknown layers, also yielded apparent porosity–thickness products individually. The existence of the buffer tank and unknown layers, mimicking unknown dead-end features, were quantitatively characterized by comparing the apparent inner diameters and porosity–thickness products, respectively.

Based on the successful validation, the potential application of the concept to hypothetical exploration has been demonstrated. Assuming an actual reservoir with four vertical faults, connected hydraulically, the synthetic observations of pressure and tracer responses were generated. The up-to-date reservoir model at each phase of the hypothetical exploration successfully reproduced the synthetic observations regardless of the accuracy of permeable structure (i.e., number of faults) if we allowed different porosity–thickness products, $\langle\phi h\rangle_P$ and $\langle\phi h\rangle_C$, to be assumed to individually reproduce pressure and tracer responses. These porosity–thickness products coincided only if the reservoir model correctly captured the permeable structure.

The logarithmic ratio $\log\left(\langle\phi h\rangle_P/\langle\phi h\rangle_C\right)$ potentially indicates the accuracy of a reservoir model to be successively updated with the progress of exploration, which will provide strategic guides for successful exploration and development at the prospect of geothermal and, potentially, general geofluid resources. For further validation, future studies will attempt to determine the evolution of $\log\left(\langle\phi h\rangle_P/\langle\phi h\rangle_C\right)$ in actual fields. A possible distribution of permeable structures can potentially be determined by modifying the reservoir

model to reproduce field observations while satisfying $\langle \phi h \rangle_P = \langle \phi h \rangle_C$. Joint application of the concept of this study and geophysical surveys will also be the subject of future studies to improve the effectiveness of exploration. Successful application will require an adequate and comprehensive understanding of hydrothermal system as in currently standard exploration and development, which includes accurately estimating total compressibility and tracer flow through nonuniform aperture distribution.

Appendix

A. Experimental Setup

The detailed specifications of the experimental apparatus (Figure 3) are described herein. The pressure gradient in a horizontal urethane tube with an inner diameter of 4 mm was controlled by adjusting the upstream and downstream header tank levels, which were connected through silicon tubes with a larger inner diameter of 9 mm to reduce pressure loss. The Reynolds numbers in the horizontal tube determined from the experimental conditions ranged from 950 to 970 approximately, which were less than the critical value of 1800 [90] for the transition between laminar and turbulent flows. During the experiments, the ambient pressure and temperature in the laboratory were 996.9 hPa and 28.8°C, respectively.

At the midpoint of the horizontal tube, a buffer tank with an inner diameter of 93 mm and height of 100 mm was connected through another urethane tube with an inner diameter of 4 mm and length of 1.5 m. Water levels in the buffer tank and downstream header tank were maintained identical. The equivalent volume of the water-filled buffer tank was varied by leveling the buffer tank to adjust the air thickness h_a. Let us assume that the mixture of water and air in the buffer tank has a bulk compressibility of $\bar{c}$ and total volume V. If the variation in the volume of this mixture caused by compression is equal to that in the equivalent volume V' filled with water, the relationship $V'/V = \bar{c}/c_w$ is satisfied, where c_w denotes the compressibility of water. Assuming uniform pressure variations in the buffer tank, the bulk compressibility $\bar{c}$ obeys the mean compressibility of water and air weighted by their volume fractions. As shown in Table 1, we determined the compressibility of water $(5.1210 \times 10^{-10} \text{ Pa}^{-1})$ using the equation of state IAPWS-IF97 [72]. The compressibility of air was assumed to be constant at $6.6401 \times 10^{-6} \text{ Pa}^{-1}$, determined at a pressure and temperature of 1013.3 hPa and 300 K, respectively [91]. The thickness of air h_a in the buffer tank was adjusted by leveling the buffer tank while closing valves A, E1, E2, F1, and F2 and opening valves B, C, D1, and D2. Valve C was opened only when the air thickness was adjusted. The buffer tank was able to be disconnected by closing valve B.

When valves E1 and E2 were closed and valves F1 and F2 were opened, the water in the interval between valves E1 and E2 was replaced with the solution of a tracer (Ponceau 4R), injected using a syringe through valve F1. Subsequently, the water originally stored in the interval was ejected through valve F2. The volumetric capacity of the interval was estimated to be 3.87 mL based on the inner diameter (4 mm) and length (300 mm) of the tube and the spacings (8 mm in total) in connectors. Approximately 10 mL of the tracer solution was injected by referring to the scale of the syringe, and the ejection of red-colored water through valve F2 was observed. After introducing the tracer solution, it was injected into the flow in the horizontal tube by closing valves D1 and D2 and simultaneously opening valves E1 and E2. The motions of these solenoid valves were electrically synchronized.

The precise distances of the pressure sensors for channels 2–4 from that for channel 1 were 2.008, 4.024, and 6.032 m, respectively, including the spacings in connectors. The precise distances of the concentration sensors for channels 2 and 3 from that for channel 1 were 3.325 and 6.238 m, respectively. The distance between the pressure and concentration sensors for channel 1 was 0.132 m. The diaphragm pressure sensors (PK025SA506, Fuji Controls Co., Ltd.) produced analog voltages ranging from 0.2 to 4.6 V, corresponding to a pressure variation of 0.0–25.0 kPaG, recorded at intervals of 1 ms using a high-speed data logger. Prior to the experiments, the voltages were calibrated and validated to reduce individual differences among sensors within 0.024 V (0.13 kPa).

We designed the in-house concentration sensors based on those presented by Takaki et al. [70]. In these sensors, green light with a peak wavelength of 520–525 nm from a light-emitting diode (DiCUNO) was transmitted through the tube and received by a phototransistor (NJL7502L, Nisshinbo Micro Devices, Inc.) with a peak sensitivity wavelength of 560 nm. Because the peak absorbance wavelength of the tracer Ponceau 4R was 508 nm [92], the voltage across a resistor connected to the emitter of the phototransistor sensitively varied depending on the tracer concentration in the tube. The recording interval of the voltage was 1 ms using the same data logger as that for the pressure sensors. The relationship between the concentration C_n (wt%) and voltage E_n (V) for channel n was calibrated using reference solutions. The relationship obeyed the following empirical expression (Figure 13 and Table 4):

$$\log C_n = a_n + b_n \log E_n + c_n (\log E_n)^2 + \frac{d_n}{\log E_n - \log E_{0n}}, \tag{A.1}$$

where a_n, b_n, c_n, and d_n denoted empirical constants and E_{0n} (V) was the voltage corresponding to pure water. The empirical constants were determined using the least squares method.

B. Similarity between the Laboratory Experiments and Reservoir Models

Similarity between the laboratory experiments (Section 3) and reservoir models (Section 5) is validated using the dimensionless expressions of the mathematical models. The dimensionless diffusion equation with respect to pressure for isothermal single-phase water is derived as follows:

$$\frac{\partial \tilde{P}}{\partial \tilde{t}} = \tilde{\kappa} \nabla^2 \tilde{P}, \tag{B.1}$$

where $\tilde{P}$ and $\tilde{t}$ are scaled pressure and time, respectively. For the laboratory experiments assuming Equation (1), we obtain the scaled diffusivity:

$$\tilde{\kappa} = \frac{ad^4}{32\mu c_w d_P^2} \bullet \frac{t_0}{l_0^2}, \tag{B.2}$$

where t_0 and l_0 are temporal and spatial scales, respectively, specified from the assumed conditions. From the correspondence between storativity $c_w \langle \phi h \rangle_P$ and $c_w d_P^2$ and that between transmissivity kh/μ and $ad^4/32\mu$, the scaled diffusivity for the reservoir models is determined as follows:

$$\tilde{\kappa} = \frac{kh}{\mu c_w \langle \phi h \rangle_P} \bullet \frac{t_0}{l_0^2}. \tag{B.3}$$

Assuming $t_0 = 10^1$ (s) and $l_0 = 10^0$ (m) for the laboratory experiments, $\tilde{\kappa}$ ranges from 10^2 to 10^7 depending on the buffer tank conditions (Table 1). The range of $\tilde{\kappa}$ from 10^3 to 10^4, assuming $t_0 = 10^7$ (s) and $l_0 = 10^3$ (m), for the reservoir models (Table 3) is within that for the laboratory experiments.

The tracer concentration approximately obeys the dimensionless advection–dispersion equation with respect to scaled concentration $\tilde{C}$ assuming incompressible flow as follows:

$$\frac{\partial \tilde{C}}{\partial \tilde{t}} + \tilde{U} \bullet \nabla \tilde{C} = \tilde{D} \nabla^2 \tilde{C}, \tag{B.4}$$

where flow velocity vector and dispersion coefficient are scaled as $\tilde{U} = U \bullet t_0 / l_0$ and $\tilde{D} = D \bullet t_0 / l_0^2$, respectively. Assuming the same temporal and spatial scales as those for the diffusion equation (Equation (B.1)), the scaled flow velocity $|\tilde{U}|$ (1.96–1.98) and dispersion coefficient $\tilde{D}$ (6.00×10^{-2}) for the laboratory experiments are comparable to those for the reservoir models $|\tilde{U}|$ (4.82) and $\tilde{D}$ (1.00×10^{-1}–1.35×10^{-1}), respectively. The flow velocity for the reservoir models refers to the travel time of 24 d estimated from the peak concentration time (Figure 10). The Peclet numbers $l_0 |\tilde{U}|/D$ for the laboratory experiments and reservoir models range from 32.7 to 33.0 and from 35.7 to 48.2, respectively.

Nomenclature

Latin Symbols

a: Modification factor for the quasi-Hagen–Poiseuille flow (-)
a_n: Empirical constant for a tracer concentration sensor (-)
b_n: Empirical constant for a tracer concentration sensor (-)
C: Tracer concentration (wt%)
C_n: Tracer concentration depending on the sensor voltage (wt%)
$\tilde{C}$: Scaled tracer concentration (-)
c_n: Empirical constant for a tracer concentration sensor (-)
c_w: Water compressibility (Pa^{-1})
$\bar{c}$: Bulk compressibility of the mixture of water and air (Pa^{-1})
D: Dispersion coefficient ($m^2 s^{-1}$)
$\tilde{D}$: Scaled dispersion coefficient (-)
d: Actual inner diameter (m)
d_C: Apparent inner diameter based on tracer responses (m)
d_n: Empirical constant for a tracer concentration sensor (-)
d_P: Apparent inner diameter based on pressure responses (m)
E_n: Voltage of a tracer concentration sensor (V)
E_{0n}: Voltage of a tracer concentration sensor corresponding to pure water (V)
h: Thickness (m)
h_a: Air thickness in the buffer tank (m)
k: Permeability (m^2)
l_0: Spatial scale (m)
P: Pressure (Pa)
$\tilde{P}$: Scaled pressure (-)
Q: Volumetric flow rate ($m^3 s^{-1}$)
r: Radial distance from the reinjection well (m)
r_w: Wellbore radius (m)
t: Time (s)
t_0: Temporal scale (s)
$\tilde{t}$: Scaled time (-)
Δt: Travel time of a tracer (s)
U: Flow velocity ($m s^{-1}$)
U: Flow velocity vector ($m s^{-1}$)
$\tilde{U}$: Scaled flow velocity vector (-)
V: Actual volume of the mixture of water and air in the buffer tank (m^3)
V': Equivalent volume of the water-filled buffer tank (m^3)
x: Distance along the tube (m).

Greek Symbols

$\tilde{\kappa}$: Scaled diffusivity (-)
μ: Water viscosity (Pa s)
ϕ: Porosity (-).

Subscripts

C: Apparent value based on tracer responses
n: Channel number for a tracer concentration sensor
P: Apparent value based on pressure responses.

Data Availability

The experimental and numerical data used to support the findings of this study have been deposited in the HydroShare repository (http://www.hydroshare.org/resource/3b66eb5ff9be4dc19d5e726bf4e08cc7).

Disclosure

This article is based on the latest version of the manuscript previously presented as preprints [93, 94].

Conflicts of Interest

The authors declare that they have no conflicts of interest.

Acknowledgments

Supplementary Materials

The supplementary photos of the experimental apparatus are presented in the Supplementary Materials provided along with this article. The photos describe the general view, main section, and pressure and concentration sensors of the apparatus in detail. (*Supplementary Materials*)

References

[1] H. S. Viswanathan, J. Ajo-Franklin, J. T. Birkholzer et al., "From fluid flow to coupled processes in fractured rock: recent advances and new frontiers," *Reviews of Geophysics*, vol. 60, no. 1, article e2021RG000744, 2022.

[2] A. Shahbazi, A. Saeidi, and R. Chesnaux, "A review of existing methods used to evaluate the hydraulic conductivity of a fractured rock mass," *Engineering Geology*, vol. 265, article 105438, 2020.

[3] T. Babadagli, "Unravelling transport in complex natural fractures with fractal geometry: a comprehensive review and new insights," *Journal of Hydrology*, vol. 587, article 124937, 2020.

[4] K. Bisdom, G. Bertotti, and H. M. Nick, "The impact of in-situ stress and outcrop-based fracture geometry on hydraulic aperture and upscaled permeability in fractured reservoirs," *Tectonophysics*, vol. 690, pp. 63–75, 2016.

[5] L. Massaro, J. Adam, and Y. Yamada, "Mechanical characterisation of new sand-hemihydrate rock-analogue material: implications for modelling of brittle crust processes," *Tectonophysics*, vol. 855, article 229828, 2023.

[6] L. Zuo, X. Tan, W. Yu, and X. Hu, "Fracture detection and numerical modeling for fractured reservoirs," *Energies*, vol. 12, no. 3, p. 386, 2019.

[7] B. Erdogmus, M. Toksoy, B. Ozerdem, and N. Aksoy, "Economic assessment of geothermal district heating systems: a case study of Balcova-Narlidere, Turkey," *Energy and Buildings*, vol. 38, no. 9, pp. 1053–1059, 2006.

[8] K. Goko, "Structure and hydrology of the Ogiri field, West Kirishima geothermal area, Kyushu, Japan," *Geothermics*, vol. 29, no. 2, pp. 127–149, 2000.

[9] A. J. Rae, D. R. Cooke, D. Phillips, and M. Zaide-Delfin, "The nature of magmatism at Palinpinon geothermal field, Negros island, Philippines: implications for geothermal activity and regional tectonics," *Journal of Volcanology and Geothermal Research*, vol. 129, no. 4, pp. 321–342, 2004.

[10] Z. Guo, R. Ma, Y. Zhang, and C. Zheng, "Contaminant transport in heterogeneous aquifers: a critical review of mechanisms and numerical methods of non-Fickian dispersion," *Science China Earth Sciences*, vol. 64, no. 8, pp. 1224–1241, 2021.

[11] T. Ptak, M. Piepenbrink, and E. Martac, "Tracer tests for the investigation of heterogeneous porous media and stochastic modelling of flow and transport—a review of some recent developments," *Journal of Hydrology*, vol. 294, no. 1-3, pp. 122–163, 2004.

[12] C. Afagwu, I. Abubakar, S. Kalam, S. F. al-Afnan, and A. A. Awotunde, "Pressure-transient analysis in shale gas reservoirs: a review," *Journal of Natural Gas Science and Engineering*, vol. 78, article 103319, 2020.

[13] I. Mohammed, T. O. Olayiwola, M. Alkathim, A. A. Awotunde, and S. F. Alafnan, "A review of pressure transient analysis in reservoirs with natural fractures, vugs and/or caves," *Petroleum Science*, vol. 18, no. 1, pp. 154–172, 2021.

[14] V. Cao, M. Schaffer, R. Taherdangkoo, and T. Licha, "Solute reactive tracers for hydrogeological applications: a short review and future prospects," *Water*, vol. 12, no. 3, p. 653, 2020.

[15] A. B. Peely, Z. Mohammadi, and E. Raeisi, "Breakthrough curves of dye tracing tests in karst aquifers: review of effective parameters based on synthetic modeling and field data," *Journal of Hydrology*, vol. 602, article 126604, 2021.

[16] Y. Zhang and T. Huang, "DNA-based tracers for the characterization of hydrogeological systems—recent advances and new frontiers," *Water*, vol. 14, no. 21, p. 3545, 2022.

[17] R. G. Agarwal, R. Al-Hussainy, and H. J. Ramey, "An investigation of wellbore storage and skin effect in unsteady liquid flow: I. Analytical treatment," *Society of Petroleum Engineers Journal*, vol. 10, no. 3, pp. 279–290, 1970.

[18] D. Bourdet, T. M. Whittle, A. A. Douglas, and Y. M. Pirard, "A new set of type curves simplifies well test analysis," *World Oil*, vol. 196, no. 6, pp. 95–101, 1983.

[19] C. V. Theis, "The relation between the lowering of the piezometric surface and the rate and duration of discharge of a well using ground water storage," *Eos, Transactions American Geophysical Union*, vol. 16, no. 2, pp. 519–524, 1935.

[20] A. F. Van Everdingen and W. Hurst, "The application of the Laplace transformation to flow problems in reservoirs," *Journal of Petroleum Technology*, vol. 1, no. 12, pp. 305–324, 1949.

[21] A. F. Van Everdingen, "The skin effect and its influence on the productive capacity of a well," *Transactions of the American Institute of Mining and Metallurgical Engineers*, vol. 5, no. 6, pp. 171–176, 1953.

[22] R. N. Horne, *Modern Well Test Analysis: A Computer-Aided Approach*, Petroway, Inc., Palo Alto, CA, 1995.

[23] O. Houzé, D. Viturat, and O. Fjaere, *Dynamic Data Analysis: The Theory and Practice of Pressure Transient, Production Analysis, Well Performance Analysis, Production Logging and the Use of Permanent Downhole Gauge Data*, KAPPA Engineering, Paris, 2012.

[24] R. DiPippo, *Geothermal Power Plants: Principles, Applications, Case Studies and Environmental Impact*, Butterworth-Heinemann, Waltham, MA, 4th edition, 2016.

[25] M. A. Grant and P. F. Bixley, *Geothermal Reservoir Engineering*, Academic Press, Burlington, MA, 2nd edition, 2011.

[26] S. J. Zarrouk and K. McLean, *Geothermal Well Test Analysis: Fundamentals, Applications and Advanced Techniques*, Academic Press, London, 2019.

[27] M. S. Hantush, "Analysis of data from pumping tests in leaky aquifers," *Eos, Transactions American Geophysical Union*, vol. 37, no. 6, pp. 702–714, 1956.

[28] G. I. Barenblatt, I. P. Zheltov, and I. N. Kochina, "Basic concepts in the theory of seepage of homogeneous liquids in fissured rocks [strata]," *Journal of Applied Mathematics and Mechanics*, vol. 24, no. 5, pp. 1286–1303, 1960.

[29] J. E. Warren and P. J. Root, "The behavior of naturally fractured reservoirs," *Society of Petroleum Engineers Journal*, vol. 3, no. 3, pp. 245–255, 1963.

[30] H. L. Cinco, F. V. Samaniego, and N. A. Dominguez, "Transient pressure behavior for a well with a finite-conductivity vertical fracture," *Society of Petroleum Engineers Journal*, vol. 18, no. 4, pp. 253–264, 1978.

[31] A. C. Gringarten, H. J. Ramey Jr., and R. Raghavan, "Unsteady-state pressure distributions created by a well with a single infinite conductivity vertical fracture," *Society of Petroleum Engineers Journal*, vol. 14, no. 4, pp. 347–360, 1974.

[32] K. Pruess and T. N. Narasimhan, "On fluid reserves and the production of superheated steam from fractured, vapor-dominated geothermal reservoirs," *Journal of Geophysical Research*, vol. 87, no. B11, pp. 9329–9339, 1982.

[33] K. Pruess and T. N. Narasimhan, "A practical method for modeling fluid and heat flow in fractured porous media," *Society of Petroleum Engineers Journal*, vol. 25, no. 1, pp. 14–26, 1985.

[34] J. A. Acuna and Y. C. Yortsos, "Application of fractal geometry to the study of networks of fractures and their pressure transient," *Water Resources Research*, vol. 31, no. 3, pp. 527–540, 1995.

[35] J. Chang and Y. C. Yortsos, "Pressure-transient analysis of fractal reservoirs," *SPE Formation Evaluation*, vol. 5, no. 1, pp. 31–38, 1990.

[36] Z. Fan and R. Parashar, "Transient flow to a finite-radius well with wellbore storage and skin effect in a poroelastic confined aquifer," *Advances in Water Resources*, vol. 142, article 103604, 2020.

[37] H. Wang, Z. Kou, J. Guo, and Z. Chen, "A semi-analytical model for the transient pressure behaviors of a multiple fractured well in a coal seam gas reservoir," *Journal of Petroleum Science and Engineering*, vol. 198, article 108159, 2021.

[38] R. Al-Hussainy, H. J. Ramey, and P. B. Crawford, "The flow of real gases through porous media," *Journal of Petroleum Technology*, vol. 18, no. 5, pp. 624–636, 1966.

[39] M. J. O'Sullivan, A. E. Croucher, E. B. Anderson, T. Kikuchi, and O. Nakagome, "An automated well-test analysis system (AWTAS)," *Geothermics*, vol. 34, no. 1, pp. 3–25, 2005.

[40] D. B. Grove and W. A. Beetem, "Porosity and dispersion constant calculations for a fractured carbonate aquifer using the two well tracer method," *Water Resources Research*, vol. 7, no. 1, pp. 128–134, 1971.

[41] O. Güven, R. W. Falta, F. J. Molz, and J. G. Melville, "A simplified analysis of two-well tracer tests in stratified aquifers," *Ground Water*, vol. 24, no. 1, pp. 63–71, 1986.

[42] S. H. Hall, "Single well tracer tests in aquifer characterization," *Ground Water Monitoring and Remediation*, vol. 13, no. 2, pp. 118–124, 1993.

[43] A. J. Hawkins, M. W. Becker, and J. W. Tester, "Inert and adsorptive tracer tests for field measurement of flow-wetted surface area," *Water Resources Research*, vol. 54, no. 8, pp. 5341–5358, 2018.

[44] M. V. Klepikova, T. le Borgne, O. Bour, M. Dentz, R. Hochreutener, and N. Lavenant, "Heat as a tracer for understanding transport processes in fractured media: theory and field assessment from multiscale thermal push-pull tracer tests," *Water Resources Research*, vol. 52, no. 7, pp. 5442–5457, 2016.

[45] A. T. Leaf, D. J. Hart, and J. M. Bahr, "Active thermal tracer tests for improved hydrostratigraphic characterization," *Ground Water*, vol. 50, no. 5, pp. 726–735, 2012.

[46] D. M. Mackay, D. L. Freyberg, P. V. Roberts, and J. A. Cherry, "A natural gradient experiment on solute transport in a sand aquifer: 1. Approach and overview of plume movement," *Water Resources Research*, vol. 22, no. 13, pp. 2017–2029, 1986.

[47] P. Reimus, G. Pohll, T. Mihevc et al., "Testing and parameterizing a conceptual model for solute transport in a fractured granite using multiple tracers in a forced-gradient test," *Water Resources Research*, vol. 39, no. 12, p. 1356, 2003.

[48] S. N. Davis, G. M. Thompson, H. W. Bentley, and G. Stiles, "Ground-water tracers — a short review," *Ground Water*, vol. 18, no. 1, pp. 14–23, 1980.

[49] M. C. Adams and J. Davis, "Kinetics of fluorescein decay and its application as a geothermal tracer," *Geothermics*, vol. 20, no. 1–2, pp. 53–66, 1991.

[50] J. A. Davis, D. B. Kent, J. A. Coston, K. M. Hess, and J. L. Joye, "Multispecies reactive tracer test in an aquifer with spatially variable chemical conditions," *Water Resources Research*, vol. 36, no. 1, pp. 119–134, 2000.

[51] A. J. Hawkins, D. Tang, R. Sinha et al., "Active tracers for hydraulic control of cooled short circuits," in *Proceedings of 48th Workshop on Geothermal Reservoir Engineering*, Stanford, CA, 2023, https://pangea.stanford.edu/ERE/pdf/IGAstandard/SGW/2023/Hawkins.pdf.

[52] D. Lemke, Z. Liao, T. Wöhling, K. Osenbrück, and O. A. Cirpka, "Concurrent conservative and reactive tracer tests in a stream undergoing hyporheic exchange," *Water Resources Research*, vol. 49, no. 5, pp. 3024–3037, 2013.

[53] A. P. Cockin, L. T. Malcolm, P. L. McGuire, R. M. Giordano, and C. D. Sitz, "Analysis of a single-well chemical tracer test to measure the residual oil saturation to a hydrocarbon miscible gas flood at Prudhoe bay," *SPE Reservoir Evaluation & Engineering*, vol. 3, no. 6, pp. 544–551, 2000.

[54] A. K. Patidar, D. Joshi, U. Dristant, and T. Choudhury, "A review of tracer testing techniques in porous media specially attributed to the oil and gas industry," *Journal of Petroleum Exploration and Production Technology*, vol. 12, no. 12, pp. 3339–3356, 2022.

[55] J. F. Tomich, R. L. Dalton Jr., H. A. Deans, and L. K. Shallenberger, "Single-well tracer method to measure residual oil saturation," *Journal of Petroleum Technology*, vol. 25, no. 2, pp. 211–218, 1973.

[56] C. V. Chrysikopoulos, "Artificial tracers for geothermal reservoir studies," *Environmental Geology*, vol. 22, no. 1, pp. 60–70, 1993.

[57] P. E. Rose, W. R. Benoit, and P. M. Kilbourn, "The application of the polyaromatic sulfonates as tracers in geothermal reservoirs," *Geothermics*, vol. 30, no. 6, pp. 617–640, 2001.

[58] B. Sanjuan, J. L. Pinault, P. Rose et al., "Tracer testing of the geothermal heat exchanger at Soultz-sous-Forêts (France) between 2000 and 2005," *Geothermics*, vol. 35, no. 5–6, pp. 622–653, 2006.

[59] A. J. Hawkins, D. B. Fox, D. L. Koch, M. W. Becker, and J. W. Tester, "Predictive inverse model for advective heat transfer in a short-circuited fracture: dimensional analysis, machine learning, and field demonstration," *Water Resources Research*, vol. 56, no. 11, article e2020WR027065, 2020.

[60] L. J. Pyrak-Nolte, N. G. W. Cook, and D. D. Nolte, "Fluid percolation through single fractures," *Geophysical Research Letters*, vol. 15, no. 11, pp. 1247–1250, 1988.

[61] K. Sawayama, T. Ishibashi, F. Jiang, T. Tsuji, and Y. Fujimitsu, "Relating hydraulic-electrical-elastic properties of natural rock

fractures at elevated stress and associated transient changes of fracture flow," *Rock Mechanics and Rock Engineering*, vol. 54, no. 5, pp. 2145–2164, 2021.

[62] D. R. Faulkner, C. A. L. Jackson, R. J. Lunn et al., "A review of recent developments concerning the structure, mechanics and fluid flow properties of fault zones," *Journal of Structural Geology*, vol. 32, no. 11, pp. 1557–1575, 2010.

[63] D. Fukuda, M. Asanuma, Y. Hishi, and K. Kotanaka, "Alcohol tracer testing at the Matsukawa vapor-dominated geothermal field, Northeast Japan," in *Proceedings of 30th Workshop on Geothermal Reservoir Engineering*, Stanford, CA, 2005.

[64] F. Óskarsson, G. P. Hersir, G. Þorgilsson, E. Júlíusson, and A. Gadalia, "Reservoir tracer test in the Krafla geothermal field using conservative and potentially degrading liquid-phase tracers," in *Proceedings of World Geothermal Congress 2020 +1*, Reykjavik, Iceland, 2020.

[65] M. van Driel, T. Renaud, M. Gravatt et al., "Numerical modelling of tracer tests in the Ohaaki geothermal system," in *Proceedings of 45th New Zealand Geothermal Workshop*, Auckland, New Zealand, 2023, http://www.geothermal-energy.org/pdf/IGAstandard/NZGW/2023/24.pdf.

[66] R. Egert, M. G. Korzani, S. Held, and T. Kohl, "Implications on large-scale flow of the fractured EGS reservoir Soultz inferred from hydraulic data and tracer experiments," *Geothermics*, vol. 84, article 101749, 2020.

[67] C. Ponte, R. Cabecas, R. Martins, G. Rangel, M. Pham, and C. Klein, "Numerical modeling for resource management at Ribeira Grande, Sao Miguel, Azores, Portugal," *Geothermal Resources Council Transactions*, vol. 33, pp. 847–854, 2009, https://publications.mygeoenergynow.org/grc/1028570.pdf.

[68] V. F. Bense, T. Gleeson, S. E. Loveless, O. Bour, and J. Scibek, "Fault zone hydrogeology," *Earth-Science Reviews*, vol. 127, pp. 171–192, 2013.

[69] J. W. Cole, D. M. Milner, and K. D. Spinks, "Calderas and caldera structures: a review," *Earth-Science Reviews*, vol. 69, no. 1-2, pp. 1–26, 2005.

[70] M. Takaki, R. Itoi, and T. Tanaka, "Laboratory experiment of tracer test in the two-dimensional heterogeneous porous medium," in *Proceedings of 40th Workshop on Geothermal Reservoir Engineering*, Stanford, CA, 2015.

[71] A. Suzuki, E. K. Bjarkason, A. Yamaguchi, A. J. Hawkins, and T. Hashida, "Estimation of flow-channel structures with uncertainty quantification: validation by 3D-printed fractures and field application," *Geothermics*, vol. 105, article 102480, 2022.

[72] International Association for the Properties of Water and Steam (IAPWS), *Revised Release on the IAPWS Industrial Formulation 1997 for the Thermodynamic Properties of Water and Steam*, International Association for the Properties of Water and Steam, Lucerne, 2007.

[73] International Association for the Properties of Water and Steam (IAPWS), *Revised Release on the IAPS Formulation 1985 for the Viscosity of Ordinary Water Substance*, International Association for the Properties of Water and Steam, Erlangen, 1997.

[74] T. Yabe and T. Aoki, "A universal solver for hyperbolic equations by cubic-polynomial interpolation I. One-dimensional solver," *Computer Physics Communications*, vol. 66, no. 2–3, pp. 219–232, 1991.

[75] T. Yabe, T. Ishikawa, P. Y. Wang, T. Aoki, Y. Kadota, and F. Ikeda, "A universal solver for hyperbolic equations by cubic-polynomial interpolation II. Two- and three-dimensional solvers," *Computer Physics Communications*, vol. 66, no. 2-3, pp. 233–242, 1991.

[76] M. Matsumoto, "A single-phase reservoir simulation method based on a roughly distributed and highly permeable fracture network model with applications to production and reinjection problems," *Geothermics*, vol. 84, article 101744, 2020.

[77] K. Pruess, C. Oldenburg, and G. Moridis, *TOUGH2 User's Guide, Version 2.0: Technical Report, No. LBNL-43134*, Lawrence Berkeley National Laboratory, University of California, Berkeley, CA, 1999.

[78] Y. J. Jung, G. S. H. Pau, S. Finsterle, and R. M. Pollyea, "TOUGH3: a new efficient version of the TOUGH suite of multiphase flow and transport simulators," *Computers & Geosciences*, vol. 108, pp. 2–7, 2017.

[79] A. Croucher, M. O'Sullivan, J. O'Sullivan, A. Yeh, J. Burnell, and W. Kissling, "Waiwera: a parallel open-source geothermal flow simulator," *Computers & Geosciences*, vol. 141, article 104529, 2020.

[80] J. A. Hoopes and D. R. F. Harleman, "Dispersion in radial flow from a recharge well," *Journal of Geophysical Research*, vol. 72, no. 14, pp. 3595–3607, 1967.

[81] E. Bresciani, R. N. Shandilya, P. K. Kang, and S. Lee, "Well radius of influence and radius of investigation: what exactly are they and how to estimate them?," *Journal of Hydrology*, vol. 583, article 124646, 2020.

[82] R. Itoi, M. Fukuda, K. Jinno, and H. Gotoh, "Interference test analysis at the Takigami geothermal field, Japan," in *Proceedings of 18th Workshop on Geothermal Reservoir Engineering*, Stanford, CA, 1993.

[83] H. Asai, S. Nakanishi, S. Tezuka et al., "Pressure interference tests at the Wasabizawa geothermal field, Akita prefecture, Japan," in *Proceedings of World Geothermal Congress 2020 +1*, Reykjavik, Iceland, 2020, http://www.geothermal-energy.org/pdf/IGAstandard/WGC/2020/22013.pdf.

[84] J. Maithya and Y. Fujimitsu, "Geophysical characterization of the Eburru geothermal field, Kenya from the analysis and interpretation of magnetotelluric and gravity techniques," in *Proceedings of World Geothermal Congress 2020+1*, Reykjavik, Iceland, 2020.

[85] C. Annison and J. Feijth, "Airborne gravity, electromagnetic and magnetic data for geothermal exploration," in *Proceedings of 44th New Zealand Geothermal Workshop*, Auckland, New Zealand, 2022.

[86] C. Kennedy, S. Henrys, and R. Kennedy, "Seismic reflection data acquisition in the Taupo Volcanic Zone: reprocessing of Broadlands Ohaaki 1984 seismic data," in *Proceedings of 45th New Zealand Geothermal Workshop*, Auckland, New Zealand, 2023.

[87] J. Kasahara, Y. Hasada, H. Mikada, H. Kuzume, H. Ohnuma, and Y. Fujise, "Seismic study at the Mori geothermal power plant, Japan using DAS and DTS in a geothermal well," in *Proceedings of 48th Workshop on Geothermal Reservoir Engineering*, Stanford, CA, 2023, https://pangea.stanford.edu/ERE/pdf/IGAstandard/SGW/2023/Kasahara.pdf.

[88] T. Li, D. Han, F. Yang et al., "Modeling study of the thermal-hydraulic-mechanical coupling process for EGS based on the framework of EDFM and XFEM," *Geothermics*, vol. 89, article 101953, 2021.

[89] P. Yu, D. Dempsey, and R. Archer, "A three-dimensional coupled thermo-hydro-mechanical numerical model with

partially bridging multi-stage contact fractures in horizontal-well enhanced geothermal system," *International Journal of Rock Mechanics and Mining Sciences*, vol. 143, article 104787, 2021.

[90] L. D. Landau and E. M. Lifshitz, "Fluid mechanics," in *Course of Theoretical Physics (Vol. 6)*, J. B. Sykes and W. H. Reid, Eds., Pergamon Press, Oxford, 2nd edition, 1987.

[91] E. W. Lemmon, R. T. Jacobsen, S. G. Penoncello, and D. G. Friend, "Thermodynamic properties of air and mixtures of nitrogen, argon, and oxygen from 60 to 2000 K at pressures to 2000 MPa," *Journal of Physical and Chemical Reference Data*, vol. 29, no. 3, pp. 331–385, 2000.

[92] K. Bevziuk, A. Chebotarev, D. Snigur, Y. Bazel, M. Fizer, and V. Sidey, "Spectrophotometric and theoretical studies of the protonation of Allura Red AC and Ponceau 4R," *Journal of Molecular Structure*, vol. 1144, pp. 216–224, 2017.

[93] M. Matsumoto and K. Sawayama, *Heterogeneity of Subsurface Pore Distribution: Characterization Based on Pressure and Tracer Responses to Identify Undiscovered Permeable Structures in Reservoirs*, 2022.

[94] M. Matsumoto and K. Sawayama, "Joint Diagnostic Approach to Pressure and Tracer Responses from Reservoirs: An Experimental and Theoretical Study to Estimate the Accuracy of Reservoir Models," 2023.